Control Engineering Practice 147 (2024) 105904

Contents lists available at ScienceDirect

Control Engineering Practice

journal homepage: www.elsevier.com/locate/conengprac

Automatic alignment of underwater snake robots operating in wakes of bluff bodies☆

Amer Orucevic *, Marianna Wrzos-Kaminska, Mads Erlend Bøe Lysø, Kristin Ytterstad Pettersen, Jan Tommy Gravdahl

Department of Engineering Cybernetics, Norwegian University of Science and Technology (NTNU), Trondheim, Norway

ARTICLE INFO

Keywords:
Marine robotics
Nonlinear control
Underwater snake robots
Autonomous underwater vehicles
Bioinspired robotics

ABSTRACT

This paper presents the development of controllers to automatically align an underwater snake robot (USR) with a wake that forms behind a bluff body, while swimming at a desired distance to the object. The low-level controllers stabilize the joint motion of the USR to a swimming gait while achieving a desired orientation and tangential velocity. The high-level controllers are designed to select references for the orientation and tangential velocity to achieve a desired placement and alignment. The control system is analyzed and proven uniformly practically asymptotically stable (UPAS). The proposed control method is validated through high-fidelity simulations that capture the intricate interaction between the USR and the surrounding fluid, and is seen to perform well in these simulations.

1. Introduction

Our understanding of the oceans is crucial for meeting challenges such as food sufficiency, bio-diversity, renewable energy, transport, and access to minerals and other resources. To fully access the vast oceans, efficient autonomous marine robots are needed. One promising approach is using USRs, which are autonomous underwater vehicles (AUVs) consisting of several slim segments connected by joints, allowing them to access narrow spaces while moving by mimicking an eel (Kelasidi, Liljebäck, Pettersen, & Gravdahl, 2016). The advantages of this design are that the robot can access narrow spaces and that, because of its articulated structure, it has the potential to interact with its environment similarly to a traditional robotic manipulator arm.

One challenge which remains to autonomous long-term operation of AUVs is power delivery. A corded power delivery solution would limit their operational area, while battery solutions put hard constraints on their operational time, and both solutions require a manned surface vessel supporting the robot. To overcome these challenges and achieve truly autonomous operation, pursuing energy autonomy is an important next step. To this end, this paper aims to develop methods that enable AUVs to harvest energy from their surroundings. Previous studies have suggested the vortex wakes which form behind bluff bodies as a promising avenue for energy harvesting in snake-like structures. Allen and Smits (2001) placed piezoelectric membranes in the wakes of bluff bodies. These snake-like structures exhibited lock-in behavior with the vortex streets, a prerequisite for achieving an optimal coupling where the structure has a minimal damping effect on the wake itself. The energy harvesting capabilities of a three-link articulated swimmer were investigated numerically through simulations by Bernier, Gazzola, Ronsse, and Chatelain (2019). The body was modeled as elliptical links connected through damped revolute joints. The study compared the energy harvested for several damping coefficients, with results indicating the existence of an optimal damping coefficient. Studies also suggest that the ability to harvest energy can improve the swimming efficiency of USRs. Wiens and Nahon (2012) explore gait optimization in order to maximize energy efficiency. A particle swarm optimization method is utilized to optimize over the parameters of a sinusoidal gait pattern, both for the cases with and without energy recovery in the joints. It is found empirically that the optimal type of gait differs significantly between the case with energy recovery and the case without. However, a simplified model is used for the fluid effects both throughout the gait optimization process and in the evaluation of the resulting gait. Bernier, Gazzola, Chatelain, and Ronsse (2018)

☆ This project has received funding from the European Research Council (ERC) under the European Union's Horizon 2020 research and innovation programme, through the ERC Advanced Grant 101017697-CRÈME. The work is also supported by the Research Council of Norway through the Centres of Excellence funding scheme, project No. 223254 – NTNU AMOS and project No. 304667.

* Corresponding author.
E-mail addresses: Amer.Orucevic@ntnu.no (A. Orucevic), Marianna.Wrzos-Kaminska@ntnu.no (M. Wrzos-Kaminska), Mads.E.B.Lyso@ntnu.no (M.E.B. Lysø), Kristin.Y.Pettersen@ntnu.no (K.Y. Pettersen), Tommy.Gravdahl@ntnu.no (J.T. Gravdahl).

https://doi.org/10.1016/j.conengprac.2024.105904
Received 30 September 2023; Received in revised form 4 March 2024; Accepted 5 March 2024
Available online 20 March 2024

use the same high-fidelity simulation method as Bernier et al. (2019) to demonstrate that a linked swimmer tracking the wake of a bluff body saves energy when compared to swimming in a free flow. The controller developed by Bernier et al. (2018) achieves tracking of the wake in the simulation. However, the stability of the control system is not proven. Furthermore, when the bluff body is allowed to move, during its motion there are large deviations in the position of the swimmer from its desired position. Orucevic, Lysø, Schmidt-Didlaukies, Pettersen and Gravdahl (2023) utilize an extremum-seeking control (ESC) scheme for systems with time-varying disturbances to find the optimal positioning of a USR online for energy harvesting in a vortex street. High-fidelity simulation results show that the USR converges to a vicinity of the optimal position.

However, approaches such as Orucevic, Lysø et al. (2023) assume that the USR is already in the vortex street. In order for the USR to transition from regular operation to energy harvesting, it is necessary to investigate ways to automatically align the USR with the wake of a bluff body from an arbitrary nearby initial position.

The control of USRs and of land-based snake robots has been studied previously with promising results (Kohl, Kelasidi, Mohammadi, Maggiore, & Pettersen, 2016; Lapierre & Jouvencel, 2005; Orucevic, Gravdahl, Pettersen, & Chaillet, 2022; Orucevic, Wrzos-Kaminska, Gravdahl and Pettersen, 2023). Orucevic et al. (2022) and Orucevic, Wrzos-Kaminska et al. (2023), presented a controller for a USR for controlling its position when swimming against an ocean current. The method is proven to render the position of the USR uniformly practically asymptotically stable (UPAS), meaning that the position converges to a neighborhood of the reference which can be arbitrarily diminished by adjusting parameters of the system. Mohammadi, Rezapour, Maggiore, and Pettersen (2016) design a controller for path following and velocity control of a land-based snake robot. The controller, which utilizes the method of virtual holonomic constraints (VHC), stabilizes motion of the snake robot to a gait behavior which is then modulated to achieve path following by means of controlling the snake robot to a desired heading and velocity. Practical stabilization of both the head angle, the tangential velocity and the speed along the path, as well as convergence to the path is shown by Mohammadi et al. (2016). Kohl et al. (2016) applied a similar controller, extended to compensate for unknown constant irrotational ocean currents, in real-life experiments to achieve path-following for a USR. Here as well, practical stabilization is achieved.

However, control strategies for USRs which do consider environmental disturbances such as ocean currents mainly focus on following a path or trajectory despite the presence of the disturbance (Kohl et al., 2016; Orucevic et al., 2022; Orucevic, Wrzos-Kaminska et al., 2023). In contrast, automatic alignment with a wake resulting from an unknown current is not easily achieved by following a prescribed path, but instead requires some other specification of the control objective. Control approaches in which the objective is to adapt a vehicle's behavior to environmental disturbances rather than resist them have been developed for traditional surface and underwater vehicles (Caharija, Pettersen, & Gravdahl, 2013; Fossen & Strand, 2001; Kim, Kim, & Sung, 2016; Kjerstad & Breivik, 2010; Pinkster & Nienhuis, 1986). Fossen and Strand (2001) present a method for positioning a surface vessel so that the mean environmental force attacks through the center line of the vessel. The method, which is denoted weather optimal position control (WOPC), enables the vessel to achieve this alignment without measuring the mean environmental force, which can be difficult or impossible in practice. The method consists of designing a control law which keeps the position of the vessel on a circle of constant radius around a point on the ocean surface, and keeps it oriented toward the point. Thinking of the environmental force as a gravitational force and the controlled vessel as a pendulum, the environmental force pushes the vessel as far downstream as possible while remaining on the circle, where the controlled heading of the vessel will align against the environmental force. It is shown that the method renders both the error in heading and the position of the vessel exponentially stable (ES). Furthermore, its efficacy is demonstrated both in simulations and experiments. However, there are a few limitations in the method's applicability to a USR. Firstly, the method as presented by Fossen and Strand (2001) assumes a fully actuated surface vessel. A USR, on the other hand, can primarily only control its heading and tangential velocity. Furthermore, these quantities cannot be controlled directly, but must be controlled through the modulation of a periodic swimming pattern. As a result, neither heading nor velocity are asymptotically stabilizable to a reference, but rather to a vicinity of the reference. Secondly, Fossen and Strand (2001) assume that the current consists solely of a component with a slowly-varying magnitude and a slowly-varying direction. While this is a reasonable simplification for a large ship, it is not necessarily as reasonable for a fairly light robot attempting to align itself in a Von Karman vortex street. Kjerstad and Breivik (2010) described a variant of the control method for vessels which are unactuated in the sway direction. However, the vessel is still assumed to have direct control authority in surge and yaw. Additionally, while non-constant, slowly varying disturbances are explored in simulations, their effect on the stability is not explored in any stability analysis. Furthermore, more general time-varying components are not considered.

This paper investigates the automatic alignment of a USR with the wake forming behind a bluff body due to an unknown, irrotational ocean current. Methods for such automatic alignment with the wake without prior knowledge of the current direction are a step towards and a prerequisite for positioning the USR in a wake in preparation for energy harvesting. A cascaded control law which aligns the USR with the wake, and enables it to automatically realign itself in the event of slowly changing directions of the average current is presented. In previous work (Orucevic, Wrzos-Kaminska et al., 2023), the control objective of tracking a predefined position reference, and the time-varying current as well as its derivative was assumed to be fully known. In this paper no knowledge or measurements of the current nor the wake it creates is required, and the controller ensures that the USR automatically positions itself downstream of a specified point, such as a bluff body, without requiring an exact position reference. Furthermore, in this paper, it is shown that the controller renders the distance between the USR and the center line of the vortex street, as well as the distance from the bluff body, UPAS, also in the presence of the time-varying current that the vortex street entails. Moreover, the proposed controllers and their analysis are based on more realistic dynamical models of the USR than those used in previous work (Orucevic, Wrzos-Kaminska et al., 2023). In addition, previous analysis of the WOPC scheme by Fossen and Strand (2001) does not include the influence of time-varying disturbances, and is performed on the dynamic model of a ship specifically. The analysis in this paper includes the presence of time-varying disturbances due to fluctuation in the current. In addition, the disturbance from a current is considered at the velocity level, making this analysis applicable to vehicles with arbitrary dynamics so long as they are equipped with lower-level controllers capable of tracking heading and forward velocity.

The strategy proposed in this paper relies on position measurements relative to an object in the environment. This is beneficial in an underwater setting, where global position measurements can be difficult to obtain. Relative position measurements, on the other hand, may be possible to obtain using a computer vision system on board, or if the object is part of a known structure, it can be equipped with a beacon for localization.

The paper is organized as follows: The model of the USR and the control of joint angles, heading, and tangential velocity are presented in Section 2. In Section 3, the design of the heading and tangential velocity references is discussed and it is proven that the proposed control system practically stabilizes the orientation and position of the USR to achieve alignment with the current at a desired distance from a bluff body. The high-fidelity simulator used to validate the control design is presented in Section 4. The simulation setup and results are discussed in Section 5. Finally, a short conclusion and discussion of future work are presented in Section 6.

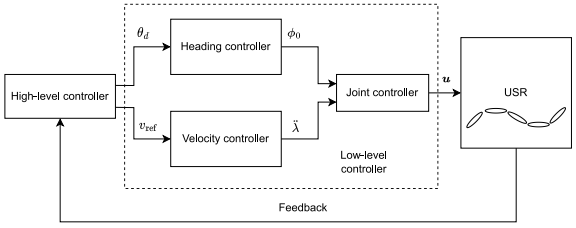

Fig. 1. Block diagram of control system.

2. Modeling and control of low-level system

The overarching control objective considered in this paper is to hold a desired distance to a bluff body while adapting to a current that may change direction over time. To achieve this, the joint angles of each link ϕ_i are controlled to follow a sinusoidal gait which has been shown to induce forward motion by Kohl, Pettersen, Kelasidi and Gravdahl (2015). The gait to be used here is referred to as the lateral undulation gait. The desired angle of each joint during this gait, for $i = 1, \dots, N_l$ being the joint number, is given by

$$\phi_{d,i} = \alpha\gamma_1(i)\sin(\lambda + (i-1)\delta) + \phi_0 \tag{1}$$

where α is the amplitude, $\gamma_1(i)$ is a scaling function that allows us to vary the amplitude along the snake body, δ is the phase shift between adjacent joints, and N_l is the number of links. The variables λ and ϕ_0 are the frequency and turning parameters. The joint reference signals are assembled into a vector $\boldsymbol{\phi}_d \in \mathbb{R}^{N_l-1}$.

The overall control system consists of two components: the low-level controller and the high-level controller. The low-level controller's main objective is to generate and follow a sinusoidal gait that achieves a desired tangential velocity v_{ref} and a desired heading θ_d. This is accomplished by utilizing the second derivative of the gait frequency $\ddot{\lambda} = u_\lambda$ and the turning parameter $\phi_0 = u_\phi$ as virtual control inputs. The high-level controller generates the desired tangential velocity and heading, designed to achieve alignment of the USR with the wake. A block diagram of the complete control system is given in Fig. 1, where the low-level controller is split into three subcomponents: a joint controller as the lowest control level, and heading and velocity controllers. In this section, the low-level controller design is presented.

2.1. Model of USR

The equations of motion for a USR which are needed for the design of this control approach, are presented in this section. A detailed model of a USR, where the full kinematics and dynamics of a planar snake robot with revolute joints are considered, is presented by Kelasidi, Pettersen, Gravdahl, Stromsoyen, and Sorensen (2017). The orientation and position along the global x- and y-axes of link i are defined as θ_i, x_i and y_i, respectively. Additionally, the position of the center of mass (CM) of the snake robot is defined as $\boldsymbol{p}_{\text{cm}} = [x_{\text{cm}}, y_{\text{cm}}]^\top$. The hydrodynamical forces along the x- and y-axes of each link i, and moments acting on it, are defined as $f_{hx,i}$, $f_{hy,i}$ and $\tau_{h,i}$, respectively. Furthermore, define $\boldsymbol{F} = [\boldsymbol{F}_x, \boldsymbol{F}_y]^\top$, where $\boldsymbol{F}_x = [f_{hx,1}, f_{hx,2}, \dots, f_{hx,N_l}]^\top$ and $\boldsymbol{F}_y = [f_{hy,1}, f_{hy,2}, \dots, f_{hy,N_l}]^\top$. To model the hydrodynamical forces, a slowly moving USR where the linear hydrodynamical drag forces and resistive torque are dominant is considered. Therefore, the nonlinear drag forces, added mass forces, and added mass inertia torques can be disregarded. The hydrodynamical forces can then be described as

$$\boldsymbol{F}_D = -\begin{bmatrix} c_t(\boldsymbol{C}_\theta)^2 + c_n(\boldsymbol{S}_\theta)^2 & (c_t - c_n)\boldsymbol{C}_\theta\boldsymbol{S}_\theta \\ (c_t - c_n)\boldsymbol{C}_\theta\boldsymbol{S}_\theta & c_t(\boldsymbol{S}_\theta)^2 + c_n(\boldsymbol{C}_\theta)^2 \end{bmatrix}\begin{bmatrix} \dot{\boldsymbol{X}}_r \\ \dot{\boldsymbol{Y}}_r \end{bmatrix} \tag{2}$$

where c_t, $c_n > 0$ are drag coefficients in the tangential and normal direction of a link, respectively, $\boldsymbol{S}_\theta = \text{diag}(\sin(\theta_1), \dots, \sin(\theta_{N_l}))$, $\boldsymbol{C}_\theta = \text{diag}(\cos(\theta_1), \dots, \cos(\theta_{N_l}))$, and

$$\dot{\boldsymbol{X}}_r = \dot{\boldsymbol{X}} - e V_x, \tag{3a}$$

$$\dot{\boldsymbol{Y}}_r = \dot{\boldsymbol{Y}} - e V_y, \tag{3b}$$

with $\boldsymbol{X} = [x_1, \dots, x_{N_l}]^\top, \boldsymbol{Y} = [y_1, \dots, y_{N_l}]^\top$, and V_x, V_y being the current in the global $x-$ and y-directions respectively. The resistive torque of the fluid is described similarly by $\boldsymbol{\tau}_{\text{hyd}} = -\boldsymbol{\Lambda}\dot{\boldsymbol{\theta}}$, where $\boldsymbol{\theta} = [\theta_1, \theta_2, \dots, \theta_{N_l}]^\top$ and $\boldsymbol{\Lambda}$ is a diagonal matrix of drag coefficients. The equations of motion are given by

$$\boldsymbol{M}_\theta\ddot{\boldsymbol{\theta}} + \boldsymbol{W}_\theta\dot{\theta}^2 + \boldsymbol{Q}_\theta(\boldsymbol{F}) + \boldsymbol{\tau}_{\text{hyd}} = \boldsymbol{D}^\top\boldsymbol{u}, \tag{4a}$$

$$\ddot{\boldsymbol{p}}_{\text{cm}} = \frac{1}{N_l m}\begin{bmatrix} \boldsymbol{e}^\top\boldsymbol{F}_{Dx} \\ \boldsymbol{e}^\top\boldsymbol{F}_{Dy} \end{bmatrix}, \tag{4b}$$

where

$$\boldsymbol{M}_\theta = J\boldsymbol{I}_{Nl} + ml^2\boldsymbol{S}_\theta\boldsymbol{V}\boldsymbol{S}_\theta + ml^2\boldsymbol{C}_\theta\boldsymbol{V}\boldsymbol{C}_\theta, \tag{5a}$$

$$\boldsymbol{W}_\theta = ml^2\boldsymbol{S}_\theta\boldsymbol{V}\boldsymbol{C}_\theta - ml^2\boldsymbol{C}_\theta\boldsymbol{V}\boldsymbol{S}_\theta, \tag{5b}$$

$$\boldsymbol{Q}_\theta(\boldsymbol{F}) = -l\boldsymbol{S}_\theta\boldsymbol{K}\boldsymbol{F}_{Dx} + l\boldsymbol{C}_\theta\boldsymbol{K}\boldsymbol{F}_{Dy}, \tag{5c}$$

$$\boldsymbol{V} = \boldsymbol{A}^\top(\boldsymbol{D}\boldsymbol{D}^\top)^{-1}\boldsymbol{A}, \tag{5d}$$

$$\boldsymbol{K} = \boldsymbol{A}^\top(\boldsymbol{D}\boldsymbol{D}^\top)^{-1}\boldsymbol{D}. \tag{5e}$$

The matrices with the subscript θ are dependent on $\boldsymbol{\theta}$, and the functional argument is omitted to conserve space. The length, mass and moment of inertia of the links are given by l, m and J, respectively. The summation vectors are defined as $\boldsymbol{e} = [1, \dots, 1]^T \in \mathbb{R}^{N_l}$ and $\bar{\boldsymbol{e}} = [1, \dots, 1]^T \in \mathbb{R}^{N_l-1}$, and the matrix $\bar{\boldsymbol{D}} = \boldsymbol{D}^T(\boldsymbol{D}\boldsymbol{D}^T)^{-1}$. The matrices $\boldsymbol{A}, \boldsymbol{D} \in \mathbb{R}^{(N_l-1)\times N_l}$ are given by $\boldsymbol{D} = \begin{bmatrix} 1 & -1 & & \\ & \ddots & \ddots & \\ & & 1 & -1 \end{bmatrix}$, $\boldsymbol{A} = \begin{bmatrix} 1 & 1 & & \\ & \ddots & \ddots & \\ & & 1 & 1 \end{bmatrix}$. The relative angle of each link can be found through the transformation

$$\bar{\boldsymbol{\phi}} = \boldsymbol{H}^{-1}\boldsymbol{\theta}, \tag{6}$$

where

$$\boldsymbol{H} = \begin{bmatrix} 1 & 1 & \dots & 1 & 1 \\ 0 & 1 & \dots & 1 & 1 \\ \vdots & & \ddots & & \vdots \\ 0 & 0 & \dots & 1 & 1 \\ 0 & 0 & \dots & 0 & 1 \end{bmatrix} \in \mathbb{R}^{N_l\times N_l}, \tag{7}$$

resulting in $\bar{\boldsymbol{\phi}} = [\phi_1, \dots, \phi_{N_l-1}, \theta_N]^\top$, with $\phi_i = \theta_i - \theta_{i+1}$. The position of the center of mass of each link can be found through the transformation

$$\boldsymbol{p} = \begin{bmatrix} \boldsymbol{X} \\ \boldsymbol{Y} \end{bmatrix} = \begin{bmatrix} -l\boldsymbol{K}^\top\cos(\boldsymbol{\theta}) + \boldsymbol{e}x_{\text{cm}} \\ -l\boldsymbol{K}^\top\sin(\boldsymbol{\theta}) + \boldsymbol{e}y_{\text{cm}} \end{bmatrix}. \tag{8}$$

Furthermore, the heading of the USR is taken to be the average orientation of the links, that is

$$\bar{\theta} = \frac{1}{N_l}\sum_{i=1}^{N_l}\theta_i. \tag{9}$$

2.2. Joint controller

The objective of the joint controller is to generate control inputs that asymptotically stabilize the joint angles of the USR to the time-varying references given by the lateral undulation gait (1). To design a joint controller it is desirable to separate the actuated and unactuated states. The states are defined as $\boldsymbol{q} = [\boldsymbol{\phi}^\top, \boldsymbol{q}_u^\top]^\top$, with the unactuated states $\boldsymbol{q}_u := [\theta_N, \boldsymbol{p}_{\text{cm}}^\top]^\top$ and actuated states $\boldsymbol{\phi} := [\phi_1, \dots, \phi_{N_l-1}]^\top$. This section follows along the approach presented by Liljebäck, Pettersen, Stavdahl, and Gravdahl (2010) to separate the dynamics. Using the

transformation between the relative link angles and global orientation (6), the model (4) can be rewritten as

$$\bar{\boldsymbol{M}}_{\bar{\phi}}\ddot{\boldsymbol{q}} + \bar{\boldsymbol{W}}_{\bar{\phi}} + \bar{\boldsymbol{Q}}_{\phi}(\boldsymbol{F}) + \bar{\boldsymbol{A}}(\boldsymbol{\tau}_{\text{hyd}}) = \bar{\boldsymbol{B}}\boldsymbol{u}, \tag{10}$$

where

$$\bar{\boldsymbol{M}}_{\bar{\phi}} = \begin{bmatrix} \boldsymbol{H}^{\top}\boldsymbol{M}_{H\bar{\phi}}\boldsymbol{H} & \boldsymbol{0}_{N_l\times 2} \\ \boldsymbol{0}_{2\times N_l} & N_l m \boldsymbol{I}_{2\times 2} \end{bmatrix}, \tag{11a}$$

$$\bar{\boldsymbol{W}}_{\phi} = \begin{bmatrix} \boldsymbol{H}^{\top}\boldsymbol{W}_{H\bar{\phi}}\text{diag}(\boldsymbol{H}\dot{\bar{\boldsymbol{\phi}}})\boldsymbol{H}\dot{\bar{\boldsymbol{\phi}}} \\ \boldsymbol{0}_{2\times 1} \end{bmatrix}, \tag{11b}$$

$$\bar{\boldsymbol{Q}}_{\phi}(\boldsymbol{F}) = \begin{bmatrix} -l\boldsymbol{H}^{\top}(\boldsymbol{S}_{H\bar{\phi}}\boldsymbol{K}\boldsymbol{F}_{Dx} - \boldsymbol{C}_{H\bar{\phi}}\boldsymbol{K}\boldsymbol{F}_{Dy}) \\ -\boldsymbol{e}^{\top}\boldsymbol{F}_{Dx} \\ -\boldsymbol{e}^{\top}\boldsymbol{F}_{Dy} \end{bmatrix}, \tag{11c}$$

$$\bar{\boldsymbol{B}} = \begin{bmatrix} \boldsymbol{I}_{(N_l-1)\times(N_l-1)} \\ \boldsymbol{0}_{3\times N_l-1} \end{bmatrix}, \tag{11d}$$

$$\bar{\boldsymbol{A}} = \begin{bmatrix} \boldsymbol{H}^{\top}\boldsymbol{\tau}_{\text{hyd}} \\ \boldsymbol{0}_{2\times 1} \end{bmatrix}. \tag{11e}$$

For matrices with subscript ϕ, the subscript replaces the functional argument ($\bar{\boldsymbol{\phi}}$) for the purpose of space conservation. The dynamics (10) can then be rewritten to

$$\bar{\boldsymbol{M}}_{11}\ddot{\bar{\boldsymbol{\phi}}} + \bar{\boldsymbol{M}}_{12}\ddot{\boldsymbol{q}}_u + \bar{\boldsymbol{W}}_1 + \boldsymbol{F}_1 + \boldsymbol{\tau}_1 = \boldsymbol{u}, \tag{12a}$$

$$\bar{\boldsymbol{M}}_{21}\ddot{\bar{\boldsymbol{\phi}}} + \bar{\boldsymbol{M}}_{22}\ddot{\boldsymbol{q}}_u + \bar{\boldsymbol{W}}_2 + \boldsymbol{F}_2 + \boldsymbol{\tau}_2 = \boldsymbol{0}_{3\times 1}, \tag{12b}$$

where the matrices from (10) have been separated into submatrices, with $\bar{\boldsymbol{M}}_{11} \in \mathbb{R}^{(N_l-1)\times(N_l-1)}$, $\bar{\boldsymbol{M}}_{12} \in \mathbb{R}^{(N_l-1)\times 3}$, $\bar{\boldsymbol{M}}_{21} \in \mathbb{R}^{3\times(N_l-1)}$ and $\bar{\boldsymbol{M}}_{22} \in \mathbb{R}^{(3\times 3)}$. Additionally, the separated Coriolis and centripetal vectors are defined as $\bar{\boldsymbol{W}}_1 \in \mathbb{R}^{(N_l-1)}$, $\bar{\boldsymbol{W}}_2 \in \mathbb{R}^3$, respectively. Furthermore, the transformed hydrodynamical forces (11c) and moments (11e) are defined as $\boldsymbol{F}_1 \in \mathbb{R}^{(N_l-1)}$, $\boldsymbol{F}_2 \in \mathbb{R}^3$, $\boldsymbol{\tau}_1 \in \mathbb{R}^{(N_l-1)}$ and $\boldsymbol{\tau}_2 \in \mathbb{R}^3$ to be, respectively. To find an expression for $\ddot{\boldsymbol{q}}_u$, (12b) is rewritten to

$$\ddot{\boldsymbol{q}}_u = -\bar{\boldsymbol{M}}_{22}^{-1}(\bar{\boldsymbol{M}}_{21}\ddot{\bar{\boldsymbol{\phi}}} + \bar{\boldsymbol{W}}_2 + \boldsymbol{F}_2 + \boldsymbol{\tau}_2). \tag{13}$$

Note that $\bar{\boldsymbol{M}}_{22}^{-1}$ is well defined as a consequence of the uniform positive definiteness of the complete system inertia matrix $\bar{\boldsymbol{M}}_{\phi}$ (Liljebäck et al., 2010). The unactuated states are substituted in (12a) by inserting (13), which results in

$$\begin{aligned}(\bar{\boldsymbol{M}}_{11} - \bar{\boldsymbol{M}}_{12}\bar{\boldsymbol{M}}_{22}^{-1}\bar{\boldsymbol{M}}_{21})\ddot{\bar{\boldsymbol{\phi}}} + \bar{\boldsymbol{W}}_1 + \boldsymbol{F}_1 \\ + \boldsymbol{\tau}_1 - \bar{\boldsymbol{M}}_{12}\bar{\boldsymbol{M}}_{22}^{-1}(\bar{\boldsymbol{W}}_2 + \boldsymbol{F}_2 + \boldsymbol{\tau}_2) = \boldsymbol{u}.\end{aligned} \tag{14}$$

The following matrix is then defined:

$$\bar{\boldsymbol{M}}_2 = \bar{\boldsymbol{M}}_{11} - \bar{\boldsymbol{M}}_{12}\bar{\boldsymbol{M}}_{22}^{-1}\bar{\boldsymbol{M}}_{21}. \tag{15}$$

Integrator backstepping is then used to design the control input $\boldsymbol{u}$. Let $\bar{\boldsymbol{\phi}}_{\text{ref}}$ be a vector with elements given by (1), and let $\tilde{\bar{\boldsymbol{\phi}}} = \bar{\boldsymbol{\phi}} - \bar{\boldsymbol{\phi}}_{\text{ref}}$. Moreover, let $\boldsymbol{z}_{\phi} = \dot{\tilde{\bar{\boldsymbol{\phi}}}} - \boldsymbol{\zeta}_{\phi}$ where $\boldsymbol{\zeta}_{\phi} = \dot{\bar{\boldsymbol{\phi}}}_{\text{ref}} - \boldsymbol{K}_{\phi,1}\tilde{\bar{\boldsymbol{\phi}}}$, and $\boldsymbol{K}_{\phi,1}$ is a positive definite matrix. The control input is selected as

$$\begin{aligned}\boldsymbol{u} = \bar{\boldsymbol{W}}_1 + \boldsymbol{F}_1 + \boldsymbol{\tau}_1 - \bar{\boldsymbol{M}}_{12}\bar{\boldsymbol{M}}_{22}^{-1}(\bar{\boldsymbol{W}}_2 + \boldsymbol{F}_2 + \boldsymbol{\tau}_2) \\ + \bar{\boldsymbol{M}}_2(\dot{\boldsymbol{\zeta}}_{\phi} - \boldsymbol{K}_{\phi,2}\boldsymbol{z}_{\phi} - \tilde{\bar{\boldsymbol{\phi}}}),\end{aligned} \tag{16}$$

where $\boldsymbol{K}_{\phi,2}$ is a positive definite matrix. Inserting the controller (16) and defining $\boldsymbol{\rho}_1 = [\tilde{\bar{\boldsymbol{\phi}}}, \boldsymbol{z}_{\phi}]^{\top}$, the following equation describes the closed-loop joint error dynamics:

$$\dot{\boldsymbol{\rho}}_1 = \begin{bmatrix} -\boldsymbol{K}_{\phi,1}\tilde{\bar{\boldsymbol{\phi}}} + \boldsymbol{z}_{\phi} \\ -\boldsymbol{K}_{\phi,2}\boldsymbol{z}_{\phi} - \tilde{\bar{\boldsymbol{\phi}}} \end{bmatrix}, \tag{17}$$

and the following proposition is made:

Proposition 1. *The system described by (17) is uniformly globally exponentially stable (UGES) at the origin.*

Proof. Consider the Lyapunov function given by $V_{\phi} = \frac{1}{2}\boldsymbol{\rho}_1^{\top}\boldsymbol{\rho}_1$. Differentiating the Lyapunov function and inserting for $\boldsymbol{\zeta}_{\phi}$ and $\boldsymbol{z}_{\phi}$ gives

$$\dot{V}_{\phi} \leq -\boldsymbol{K}_{\phi,1}\tilde{\bar{\boldsymbol{\phi}}}^2 - \boldsymbol{K}_{\phi,2}\boldsymbol{z}_{\phi}^2 \tag{18}$$

By (Khalil, 2002, Theorem 4.10), the origin of the system is UGES.

2.3. Simplified model of USR following a swimming gait

The complexity of the model presented in Section 2.1 makes it challenging to use for design of heading and velocity controllers for the USR as a whole. Therefore, a control-oriented model was developed for USRs exposed to currents, approximating the revolute joint motion with prismatic joints by Kohl, Kelasidi, Pettersen and Gravdahl (2015), with the aim to capture the qualitative behavior of the complex model. The assumption in this model is that the currents are time-invariant and irrotational. However, still it includes cross-terms between states, reflecting the intricate dependencies between the link motion and tangential and normal velocities. To achieve reference tracking for the heading and tangential velocity and develop controllers for this control-oriented model, it is often necessary to cancel these terms. Furthermore, the currents in a wake behind a bluff body are highly time-varying and rotational. Therefore, the parameters identified for the hydrodynamical drag and resistive torques by Kohl, Kelasidi et al. (2015) will likely not give a good approximation of the hydrodynamical forces that affect the USR during operations in a wake. As discussed by Orucevic, Wrzos-Kaminska et al. (2023), attempts to cancel poorly approximated terms, may result in degraded performance. Therefore, this paper proposes that during sinusoidal motion, the whole USR is considered a single rigid body with $\ddot{\lambda} = u_{\lambda}$ and $\phi_0 = u_{\phi}$ as control inputs for the tangential velocity and angular motion, respectively. The current velocity in the global frame is denoted as $\boldsymbol{V}_c(t)$. The tangential and normal velocity components of the USR and current, given in the body frame of the USR, are defined as v_t, v_n, $V_{ct}(t)$ and $V_{cn}(t)$, respectively. The relation between $\boldsymbol{V}_c(t)$, $V_{ct}(t)$ and $V_{cn}(t)$ is:

$$\begin{bmatrix} V_{ct}(t) \\ V_{cn}(t) \end{bmatrix} = \boldsymbol{R}(\bar{\theta})^{\top}\boldsymbol{V}_c(t) \tag{19}$$

where $\boldsymbol{R}(\cdot)$ denotes the two-dimensional rotation matrix:

$$\boldsymbol{R}(x) = \begin{bmatrix} \cos(x) & -\sin(x) \\ \sin(x) & \cos(x) \end{bmatrix} \tag{20}$$

The following assumptions are made:

Assumption 1. The USR is following the sinusoidal gait given by (1).

Assumption 1 constitutes the premise for constructing a simplified model of the dynamics of the USR as a whole while its motion follows a certain pattern, namely gaits which can be described by (1). A USR with no other actuators than those of its joints is dependent on following some motion pattern to produce any forward locomotion (Pettersen, 2017). While other gaits resulting in forward motion than those encompassed by (1) may exist, this paper focuses on those described by (1) which encompasses a spectrum of bio-inspired gaits, including snake- and eel-like motion.

Assumption 2. The USR is moving against the current such that $(v_t - V_{ct}(t)) > 0$.

Assumption 3. The current velocity $\boldsymbol{V}_c(t)$ and its derivative are bounded by V_M, $V_{M,d} > 0$ such that $\|\boldsymbol{V}_c(t)\| \leq V_M$, $\|\dot{\boldsymbol{V}}_c(t)\| \leq V_{M,d}$.

As seen from the control-oriented model of Kohl, Kelasidi et al. (2015), the USR can only turn while the relative tangential velocity is non-zero. Therefore, Assumption 2 ensures that the USR can turn. Because the objective of this controller is to align the USR with the

wake of a bluff body, the USR will likely operate such that it is moving against the current, in which case Assumption 2 is satisfied. Note that control authority is only held over the turning rate of the USR and the tangential velocity v_t. The control objective is to stabilize the heading dynamics and the absolute tangential velocity dynamics to their references. Since there is no control authority over the velocity of the USR in the normal direction, it can at best be expected to consist of only a small contribution from the swimming motion, such that it ends up approximately following the current velocity. This is equivalent to the relative normal velocity being close to 0. To this end, the absolute tangential velocity v_t and the normal velocity relative to the ocean current $v_{n,\text{rel}} = v_n - V_{cn}(t)$ instead of v_n, are analyzed. The resulting simplified model is given by

$$\ddot{\bar{\theta}} = -\lambda_\theta \dot{\bar{\theta}} + f_\theta \phi_0 + d_\theta(\tilde{\boldsymbol{\phi}}) + d_1(t), \tag{21a}$$

$$\dot{v}_t = -\lambda_t (v_t - V_{ct}(t)) + f_t \ddot{\lambda} + d_t(\tilde{\boldsymbol{\phi}}) + d_2(t) \tag{21b}$$

$$\dot{v}_{n,\text{rel}} = -\lambda_n v_{n,\text{rel}} + d_n(\tilde{\boldsymbol{\phi}}) + d_3(t) - \dot{V}_{cn}(t), \tag{21c}$$

where $f_t > 0$ and $f_\theta > 0$. Furthermore, λ_θ, λ_t, $\lambda_n > 0$ are the drag coefficients for the average angular velocity, tangential velocity, and normal velocity, respectively. The unmodeled dynamics and time-varying disturbances are given by $d_1(t)$, $d_2(t)$ and $d_3(t)$, and are assumed to be bounded.

Assumption 4. For any $\Delta > 0$ such that $\| \left[\bar{\theta},\ \dot{\bar{\theta}},\ v_t,\ v_{n,\text{rel}}\right]^\top \| \leq \Delta$, there exists a bound $d_\Delta > 0$ such that $|d_1(t)| + |d_2(t)| + |d_3(t)| \leq d_\Delta$.

Disturbances that result from the USR deviating from the sinusoidal gait (1) are given by $d_\theta(\cdot)$, $d_t(\cdot)$ and $d_n(\cdot)$, which are gathered in the vector $\boldsymbol{d}_\phi(\tilde{\boldsymbol{\phi}})$. The functions are continuous and satisfy $\boldsymbol{d}_\phi(0) = 0$. Additionally, the following assumption is made:

Assumption 5. The disturbances that result from deviation from the sinusoidal gait (1) are bounded such that $\|\boldsymbol{d}_\phi(\tilde{\boldsymbol{\phi}})\| \leq \alpha_\phi(\|\tilde{\boldsymbol{\phi}}\|)$, where $\alpha_\phi(\cdot)$ is a class $\mathcal{K}$-function.

Remark 1. The unmodeled dynamics encompassed by $d_1(t), d_2(t), d_3(t)$ are comprised of various phenomena, including nonlinear drag, added mass effects, and cross-terms through which the states influence each other due to effects arising from drag and the sinusoidal motion. At lower velocities and accelerations, linear drag tends to dominate over the contributions of nonlinear drag and added mass. Additionally, the average impact of the cross-terms stemming from sinusoidal motion diminishes significantly when the turning offset ϕ_0 remains small. Moreover, for bounded velocities and accelerations, the hydrodynamical terms remain within bounds as well. In addition, it is reasonable to assume that the rate of change of the current velocities is bounded. Hence, as stated in Assumption 4, the hydrodynamical forces and other disturbances remain bounded. Furthermore, from Proposition 1 it follows that the joint error $\tilde{\boldsymbol{\phi}}$ is bounded and converges exponentially to zero. Thus the validity of Assumption 5 is reinforced.

2.4. Stabilization of the simplified control-model

Let v_{ref}, θ_{ref} be references for the tangential (i.e. forward) velocity and heading, respectively. It is assumed that the references and their derivatives are bounded. The objective of this low-level controller is to track the desired heading and tangential velocity. Meanwhile, the unactuated normal velocity stabilizes to the ocean current. For the heading, a backstepping approach is utilized to design the control input u_ϕ. To this end, the error $z_1 := \bar{\theta} - \theta_{\text{ref}}$, $z_2 := \dot{\bar{\theta}} - \zeta_1$, are defined, where ζ_1 is a reference angular velocity and serves as a virtual control input. The derivatives of z_1 and z_2 are given by

$$\begin{aligned} \dot{z}_1 &= \zeta_1 - \dot{\theta}_{\text{ref}} + z_2 \\ \dot{z}_2 &= -\lambda_\theta \dot{\bar{\theta}} + f_\theta \varphi_0 + d_\theta(\tilde{\boldsymbol{\phi}}) + d_1(t) - \dot{\zeta}_1. \end{aligned} \tag{22}$$

In addition, the velocity error variable is defined as $\tilde{v}_t = v_t - v_{\text{ref}}$. The control inputs are selected as

$$\zeta_1 = \dot{\theta}_{\text{ref}} - k_{\theta,1} z_1 \tag{23a}$$

$$u_\phi = -k_{\theta,2} z_2 + \frac{1}{f_\theta}\dot{\zeta}_1 + \frac{\lambda_\theta}{f_\theta}\zeta_1 - \frac{1}{f_\theta} z_1 \tag{23b}$$

$$u_\lambda = \frac{\lambda_t}{f_t} v_{\text{ref}} - k_v \tilde{v}_t + \dot{v}_{\text{ref}}, \tag{23c}$$

where the control gains are given by $k_{\theta,1} > 0$, $k_{\theta,2} > 0$ and $k_v > 0$. Inserting (23) into (21b) and (22) gives, together with (21c), the closed-loop dynamics

$$\dot{z}_1 = -k_{\theta,1} z_1 + z_2 \tag{24a}$$

$$\dot{z}_2 = -(f_\theta k_{\theta,1} + \lambda_\theta) z_2 - z_1 + d_1(t) + d_\theta(\tilde{\boldsymbol{\phi}}) \tag{24b}$$

$$\dot{\tilde{v}}_t = -(f_t k_v + \lambda_t)\tilde{v}_t + d_2(t) + \lambda_t V_{ct}(t) + d_t(\tilde{\boldsymbol{\phi}}) \tag{24c}$$

$$\begin{aligned} \dot{v}_{n,\text{rel}} = {} & -\lambda_n v_{n,\text{rel}} + d_n(\tilde{\boldsymbol{\phi}}) + d_3(t) \\ & + (z_2 + \dot{\theta}_d - k_{\theta,1} z_1)\left[\cos(\bar{\theta}) \quad \sin(\bar{\theta})\right] \boldsymbol{V}_c(t) \\ & - \left[-\sin(\bar{\theta}) \quad \cos(\bar{\theta})\right] \dot{\boldsymbol{V}}_c(t), \end{aligned} \tag{24d}$$

which can be written as

$$\begin{bmatrix} \dot{z}_1 \\ \dot{z}_2 \\ \dot{\tilde{v}}_t \\ v_{n,\text{rel}} \end{bmatrix} = \overbrace{\begin{bmatrix} -k_{\theta,1} & 1 & 0 & 0 \\ -1 & -(f_\theta k_{\theta,2} + \lambda_\theta) & 0 & 0 \\ 0 & 0 & -(f_t k_v + \lambda_t) & 0 \\ -k_{\theta,1} V_{ct}(t) & V_{ct}(t) & 0 & -\lambda_n \end{bmatrix}}^{:=\boldsymbol{A}_l(t)} \begin{bmatrix} z_1 \\ z_2 \\ \tilde{v}_t \\ v_{n,\text{rel}} \end{bmatrix} + \underbrace{\begin{bmatrix} 0 \\ d_1(t) \\ d_2(t) + \lambda_t V_{ct}(t) \\ d_3(t) + \dot{\theta}_d V_{ct}(t) - \left[-\sin(\bar{\theta}) \quad \cos(\bar{\theta})\right] \dot{\boldsymbol{V}}_c(t) \end{bmatrix}}_{:=\boldsymbol{d}(t)} + \begin{bmatrix} 0 \\ d_\theta(\tilde{\boldsymbol{\phi}}) \\ d_t(\tilde{\boldsymbol{\phi}}) \\ d_n(\tilde{\boldsymbol{\phi}}) \end{bmatrix} \tag{25}$$

The complete system, consisting of joint, heading and velocity controllers, can be considered a cascaded system where the driving system is given by (17) and the driven system is (25). Furthermore, the parameter vector is defined as $\boldsymbol{\varphi}_l = [k_{\theta,1}, k_{\theta,2}, k_v, \lambda_n]^\top$, which belongs to $\Theta_l = \mathbb{R}^4_{>0}$. The following proposition is made

Proposition 2. *The cascaded system (17) and (25) is UPAS on the set of admissible parameters Θ_l for bounded references.*

Proof. First, the nominal part of (25) is considered,

$$\dot{\boldsymbol{e}}_l = \boldsymbol{A}_l(t)\boldsymbol{e}_l + \boldsymbol{d}(t). \tag{26}$$

A Lyapunov function is defined as

$$\mathcal{V}_l = \frac{1}{2}\boldsymbol{e}_l^\top \boldsymbol{e}_l. \tag{27}$$

Differentiating $\mathcal{V}_l$ gives

$$\begin{aligned} \dot{\mathcal{V}}_l = {} & -k_{\theta,1} z_1^2 - (f_\theta k_{\theta,2} + \lambda_\theta) z_2^2 - (f_t k_v + \lambda_t)\tilde{v}_t^2 \\ & - \lambda_n v_{n,\text{rel}}^2 + v_{n,\text{rel}}\left(z_2 - k_{\theta,1} z_1\right) V_{ct}(t) + \boldsymbol{e}_l^\top \boldsymbol{d}(t). \end{aligned} \tag{28}$$

Consider now the bounded local domain. For bounded states $\boldsymbol{e}_l$, since v_{ref}, θ_{ref}, $\dot{\theta}_{\text{ref}}$ are bounded by assumption, $\bar{\theta}$, $\dot{\bar{\theta}}$ and v_t, are also bounded. Then by Assumption 4 there exists a bound d_Δ such that $|d_1(t)| + |d_2(t)| + |d_3(t)| \leq d_\Delta$. Furthermore, from Assumption 3, the current velocities are bounded. Finally, by using Young's inequality on the term $v_{n,\text{rel}}\left(z_2 - k_{\theta,1} z_1\right) V_{ct}(t)$, the following bound can be found:

$$\begin{aligned} \dot{\mathcal{V}}_l \leq {} & -k_{\theta,1}\left(1 - \frac{V_M \gamma_1}{2}\right) z_1^2 - \left((f_\theta k_{\theta,2} + \lambda_\theta) - \frac{V_M \gamma_2}{2}\right) z_2^2 \\ & - (f_t k_v + \lambda_t)\tilde{v}_t^2 - \left(\lambda_n - \frac{k_{\theta,1} V_M}{2\gamma_1} - \frac{V_M}{2\gamma_2}\right) v_{n,\text{rel}}^2 \\ & + \left(d_\Delta + \lambda_t V_M + V_{M,d} + |\dot{\theta}_{\text{ref}}| V_M\right) \|\boldsymbol{e}_l\|. \end{aligned} \tag{29}$$

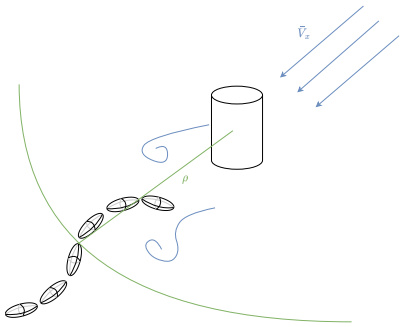

Fig. 2. Illustration of USR operating in the wake behind a cylinder.

The bound (29) is negative for $\|\boldsymbol{e}_l\| > \frac{B_2}{B_1(\boldsymbol{\varphi}_l)}$, where

$$B_1(\boldsymbol{\varphi}_l) = \min\left\{ k_{\theta,1}\left(1 - \frac{V_M\gamma_1}{2}\right), (f_t k_v + \lambda_t), \left((f_\theta k_{\theta,2} + \lambda_\theta) - \frac{V_m\gamma_2}{2}\right), \lambda_n \right\}, \tag{30a}$$

$$B_2(\boldsymbol{\varphi}_l) = d_\Delta + V_{M,d} + \lambda_t V_M + |\dot{\theta}_{\text{ref}}| V_M, \tag{30b}$$

where $B_1(\cdot)$ can be increased or decreased by adjusting the parameters $\boldsymbol{\varphi}_l$.

Hence (Orucevic, Wrzos-Kaminska et al., 2023, Assumption 3) is satisfied, and by Assumption 5, (Orucevic, Wrzos-Kaminska et al., 2023, Assumption 1) is also satisfied. Finally, since the driving system (17) is UGES which is a stronger property than UPAS, the conditions of (Orucevic, Wrzos-Kaminska et al., 2023, Theorem 2) are satisfied and the cascaded system (17) and (25) is UPAS on the set of admissible parameters Θ_l.

3. Modeling and control of high-level system

The high-level control takes its inspiration from Fossen and Strand (2001), Kjerstad and Breivik (2010). However, in both of these papers a virtual point is chosen for the vessel to revolve around, and the point must subsequently be updated in order for the vessel to stay in one spot while aligning its heading against the disturbance. However, in this paper, the ultimate objective is to ensure that the USR ends up in the wake of a bluff body and tracks slow changes in the direction of this wake automatically. Firstly, as the system in question is underwater, the mean environmental force in Fossen and Strand (2001) is replaced by an ocean current, and will be treated at the kinematic level. Secondly, it is assumed that the ocean current can be described by a mean component and its direction, both of which are constant or slowly-varying, onto which a smaller, general time-varying component is added. This smaller component is by definition zero-mean, as it is added to the mean of the current. The vortex street of a bluff body is generated exactly downstream of the bluff body with respect to the current, so that the center-line of the vortex street is parallel with the current direction. Thus, stabilizing the position of the USR to a vicinity of the vortex street center-line is equivalent to stabilizing it to a vicinity of the downstream direction from the bluff body . Finally, note that the point around which the USR should revolve is constant and given by the centroid of the bluff body, in order to end up downstream from it in a similar way to the surface vessel of Fossen and Strand (2001). Thus, only weather optimal heading control (WOHC), where the position of the hinge point is kept constant, is relevant as a starting point for the method presented in this paper. The concept is illustrated in Fig. 2.

This section introduces control laws which generate heading and tangential velocity references for the USR. These control laws are designed to point the USR towards the bluff body and make its position converge to a circle of prescribed radius. Moreover, by employing Lyapunov analysis it is shown that this choice of references renders the position of the USR UPAS, provided that the references are followed sufficiently well by low-level controllers. This is the case when using the low-level controllers from Section 2, by Proposition 2.

3.1. Modeling of the kinematics

Fossen and Strand (2001) model the total environmental disturbance as a force acting on a surface vessel, and consists of the total influence from wind, waves and current. In the absence of wind as is the case for an underwater robot, the disturbance from the current can be modeled as a velocity.

Remark 2. Modeling the disturbance as a velocity rather than a force influencing the dynamics of the robot corresponds to assuming that the USR is swept along with the changes in the current instantaneously. This would be the case for a very light system. Comparing this to a linear drag model, the effect of the current on the robot velocity would be of first order, with the robot dynamics acting as a low-pass filter. Thus, the model used here represents a worst-case scenario with respect to the influence of time-varying current components on the robot velocity. The benefit of this approach is that the analysis becomes more modularized, so that the results from the analysis of the high-level controller are applicable to any underwater system equipped with controllers for heading and tangential velocity.

The derivative of the position of the CM of the USR, given in terms of the absolute tangential velocity v_t and relative normal velocity $v_{n,\text{rel}}$ of the USR is given by

$$\begin{aligned}\dot{\boldsymbol{p}}_{\text{cm}} &= \boldsymbol{R}(\tilde{\theta}) \begin{bmatrix} v_t \\ v_{n,\text{rel}} + V_{cn}(t) \end{bmatrix} \\ &= \boldsymbol{R}(\tilde{\theta}) \left(\begin{bmatrix} v_t \\ v_{n,\text{rel}} \end{bmatrix} + \begin{bmatrix} 0 & 0 \\ 0 & 1 \end{bmatrix} \boldsymbol{R}^\top(\tilde{\theta}) \boldsymbol{V}_c(t) \right)\end{aligned} \tag{31}$$

where $\boldsymbol{V}_c(t)$ is the time-varying ocean current given in the global frame. The current $\boldsymbol{V}_c(t)$ can be described as

$$\boldsymbol{V}_c(t) = \boldsymbol{R}(\beta_c) \left(\begin{bmatrix} \bar{V}_x \\ 0 \end{bmatrix} + \begin{bmatrix} \tilde{V}_x(t) \\ \tilde{V}_y(t) \end{bmatrix} \right) \tag{32}$$

where β_c and $\bar{V}_x$ are constant or slowly varying, and the time varying-components $\tilde{V}_x(t)$, $\tilde{V}_y(t)$ satisfy $|\tilde{V}_x(t)| \leq \tilde{V}_{x,\max}$, $|\tilde{V}_y(t)| \leq \tilde{V}_{y,\max}$ for some $\tilde{V}_{x,\max}, \tilde{V}_{y,\max} > 0$, and $\tilde{V}_{x,\max} < \bar{V}_x$.

Remark 3. Having a somewhat steady current direction is necessary for the formation of a proper Von Karman vortex street. Thus, under conditions where there exists a vortex street for the USR to align with, it is reasonable to assume that β_c is constant.

Remark 4. In the case of a wake behind an object, a more precise description of the current would be as a time-varying vector field $\boldsymbol{V}_c(t, p)$, which is periodic at a fixed point $\boldsymbol{p}$ in the case of a steady wake. In the case of a current described by a vector field, $\boldsymbol{V}_c(t) = \boldsymbol{V}_c(t, p(t))$ can be treated as the current along a trajectory $\boldsymbol{p}(t)$ of the system. Directly behind the cylinder, the average of $\tilde{V}_y(t)$ will be 0 over one period.

As in Fossen and Strand (2001), the position of the robot is described in polar coordinates, but the origin is placed at a fixed object (e.g. a cylinder). The objective is to have the position of the snake robot converge to a desired constant distance ρ_d downstream from the object.

Let ρ be the radius and γ the angle of the polar coordinates, so that

$$\begin{bmatrix} x_{\text{cm}} \\ y_{\text{cm}} \end{bmatrix} = \begin{bmatrix} \rho\cos(\gamma) \\ \rho\sin(\gamma) \end{bmatrix}. \tag{33}$$

By differentiating ρ, γ, the following kinematic relation can be derived:

$$\begin{bmatrix}\dot{\rho}\\ \dot{\gamma}\end{bmatrix} = \begin{bmatrix}1 & 0\\ 0 & \frac{1}{\rho}\end{bmatrix} \boldsymbol{R}^{\top}(\gamma)\boldsymbol{R}(\bar{\theta})\left(\begin{bmatrix}v_t\\ v_{n,\mathrm{rel}}\end{bmatrix} + \begin{bmatrix}0 & 0\\ 0 & 1\end{bmatrix} \boldsymbol{R}^{\top}(\bar{\theta})\boldsymbol{V}_c(t)\right) \tag{34}$$

for $\rho \neq 0$.

Remark 5. Since the origin is at the position of an object in the environment, $\rho = 0$ is highly undesirable in any case, as it would lead to a collision with the object. Thus, requiring $\rho \neq 0$ is not restrictive for a practical application, and the analysis shows that it can also be avoided through a proper choice of initial states and parameters.

3.2. Heading and velocity reference selection and analysis

As in Fossen and Strand (2001), the heading reference is chosen to be inwards towards the origin, i.e.

$$\theta_{\mathrm{ref}} = \gamma + \pi. \tag{35}$$

Inserting $v_t = v_{\mathrm{ref}} + \tilde{v}_t$, $\bar{\theta} = \theta_{\mathrm{ref}} + \tilde{\theta}$, (35) and (32), (34) can be written as

$$\begin{aligned}\begin{bmatrix}\dot{\rho}\\ \dot{\gamma}\end{bmatrix} = &\begin{bmatrix}1 & 0\\ 0 & \frac{1}{\rho}\end{bmatrix}\left(-\boldsymbol{R}(\tilde{\theta})\begin{bmatrix}v_{\mathrm{ref}}+\tilde{v}_t\\ v_{n,\mathrm{rel}}\end{bmatrix}\right.\\ &\left. + \boldsymbol{R}(\tilde{\theta})\begin{bmatrix}0 & 0\\ 0 & 1\end{bmatrix}\boldsymbol{R}^{\top}(\tilde{\theta})\boldsymbol{R}^{\top}(\gamma-\beta_c)\begin{bmatrix}\bar{V}_x+\tilde{V}_x\\ \tilde{V}_y\end{bmatrix}\right).\end{aligned} \tag{36}$$

Define the error variables $\tilde{\gamma} = \gamma - \beta_c$, and $\tilde{\rho} = \rho - \rho_d$. Setting $\dot{\beta}_c = 0$, the resulting error dynamics are given by

$$\begin{aligned}\begin{bmatrix}\dot{\tilde{\rho}}\\ \dot{\tilde{\gamma}}\end{bmatrix} = &\begin{bmatrix}-v_{\mathrm{ref}}\\ 0\end{bmatrix} + \begin{bmatrix}1 & 0\\ 0 & \frac{1}{\rho_d+\tilde{\rho}}\end{bmatrix}\left(\left(\begin{bmatrix}0 & 0\\ 0 & 1\end{bmatrix} + \boldsymbol{T}(\tilde{\theta})\right)\boldsymbol{R}^{\top}(\tilde{\gamma})\begin{bmatrix}\bar{V}_x+\tilde{V}_x\\ \tilde{V}_y\end{bmatrix}\right.\\ &\left. + (I-\boldsymbol{R}(\tilde{\theta}))\begin{bmatrix}v_{\mathrm{ref}}\\ 0\end{bmatrix} - \boldsymbol{R}(\tilde{\theta})\begin{bmatrix}\tilde{v}_t\\ v_{n,\mathrm{rel}}\end{bmatrix}\right)\end{aligned} \tag{37}$$

where

$$\boldsymbol{T}(\tilde{\theta}) = \begin{bmatrix}\sin^2(\tilde{\theta}) & -\sin(\tilde{\theta})\cos(\tilde{\theta})\\ -\sin(\tilde{\theta})\cos(\tilde{\theta}) & -\sin^2(\tilde{\theta})\end{bmatrix}. \tag{38}$$

The reference velocity, v_{ref}, is chosen as

$$v_{\mathrm{ref}} = k_\rho \cos(\tilde{\theta})\tilde{\rho}. \tag{39}$$

As in Kjerstad and Breivik (2010), the error term is scaled by $\cos(\tilde{\theta})$ to avoid unnecessary and undesired control effort while the heading is not as desired. This corresponds to using only the part of the error that is parallel to the body x-axis of the system, in other words the error in the actuated direction.

The dynamics (37) in closed loop with (35) and (39) become

$$\begin{aligned}\dot{\tilde{\rho}} = &-k_\rho\tilde{\rho} + \left(s_{\tilde{\theta}}^2 c_{\tilde{\gamma}} + s_{\tilde{\theta}}c_{\tilde{\theta}}s_{\tilde{\gamma}}\right)\left(\bar{V}_x+\tilde{V}_x\right)\\ &+ \left(s_{\tilde{\theta}}^2 s_{\tilde{\gamma}} - s_{\tilde{\theta}}c_{\tilde{\theta}}c_{\tilde{\gamma}}\right)\tilde{V}_y + s_{\tilde{\theta}}^2 k_\rho\tilde{\rho} - c_{\tilde{\theta}}\tilde{v}_t + s_{\tilde{\theta}}v_{n,\mathrm{rel}}\end{aligned} \tag{40a}$$

$$\begin{aligned}\dot{\tilde{\gamma}} = &\frac{1}{\tilde{\rho}+\rho_d}\left(-s_{\tilde{\gamma}}\left(\bar{V}_x+\tilde{V}_x\right) + \left(s_{\tilde{\theta}}^2 s_{\tilde{\gamma}} - s_{\tilde{\theta}}c_{\tilde{\theta}}c_{\tilde{\gamma}}\right)\left(\bar{V}_x+\tilde{V}_x\right)\right.\\ &\left.\left(s_{\tilde{\theta}}^2 c_{\tilde{\gamma}} + s_{\tilde{\theta}}c_{\tilde{\theta}}s_{\tilde{\gamma}}\right)\tilde{V}_y - s_{\tilde{\theta}}\left(k_\rho c_{\tilde{\theta}}\tilde{\rho} + \tilde{v}_t\right) - c_{\tilde{\theta}}v_{n,\mathrm{rel}} + c_{\tilde{\gamma}}\tilde{V}_y\right)\end{aligned} \tag{40b}$$

where $\cos(\tilde{\gamma})$ and $\sin(\tilde{\gamma})$ are denoted as $c_{\tilde{\gamma}}$ and $s_{\tilde{\gamma}}$, respectively, and similarly for $\tilde{\theta}$, for the sake of brevity.

Let $\boldsymbol{\xi} = \left[\tilde{v}_t, v_{n,\mathrm{rel}}, \tilde{\theta}, \dot{\tilde{\theta}}, \boldsymbol{\varrho}_1^{\top}\right]^{\top}$, and let k_ρ, $\varphi_\gamma = \frac{\bar{V}_{y,\max}}{\bar{V}_x - \bar{V}_{x,\max}}$ be parameters of the system. The system (40) may then be rewritten as

$$\dot{\tilde{\gamma}} = f_1\left(t,\tilde{\rho},\tilde{\gamma},\varphi_\gamma\right) + \boldsymbol{g}_1\left(t,\tilde{\rho},\tilde{\gamma},\boldsymbol{\xi},k_\rho\right)\boldsymbol{\xi} \tag{41a}$$

$$\dot{\tilde{\rho}} = f_2\left(\tilde{\rho},k_\rho\right) + \boldsymbol{g}_2\left(t,\tilde{\rho},\tilde{\gamma},\boldsymbol{\xi},k_\rho\right)\boldsymbol{\xi} \tag{41b}$$

where

$$f_1 = \frac{1}{\tilde{\rho}+\rho_d}\left(-s_{\tilde{\gamma}}\left(\bar{V}_x+\tilde{V}_x\right) + c_{\tilde{\gamma}}\tilde{V}_y\right) \tag{41c}$$

$$\boldsymbol{g}_1 = \frac{1}{\tilde{\rho}+\rho_d}\left[-s_{\tilde{\theta}},\quad -c_{\tilde{\theta}},\quad \frac{s_{\tilde{\theta}}}{\tilde{\theta}}g_{13},\quad 0,\quad \boldsymbol{0}_{1\times 2(N_l-1)}\right] \tag{41d}$$

$$g_{13} = \left(-c_{\tilde{\theta}}k_\rho\tilde{\rho} + \left(s_{\tilde{\theta}}s_{\tilde{\gamma}} - c_{\tilde{\theta}}c_{\tilde{\gamma}}\right)\left(\bar{V}_x+\tilde{V}_x\right) - \left(s_{\tilde{\theta}}c_{\tilde{\gamma}} + c_{\tilde{\theta}}s_{\tilde{\gamma}}\right)\tilde{V}_y\right) \tag{41e}$$

$$f_2 = -k_\rho\tilde{\rho} \tag{41f}$$

$$\boldsymbol{g}_2 = \left[-c_{\tilde{\theta}},\quad s_{\tilde{\theta}},\quad \frac{s_{\tilde{\theta}}}{\tilde{\theta}}g_{23},\quad 0,\quad \boldsymbol{0}_{1\times 2(N_l-1)}\right] \tag{41g}$$

$$g_{23} = \left(s_{\tilde{\theta}}k_\rho\tilde{\rho} + \left(s_{\tilde{\theta}}c_{\tilde{\gamma}} + c_{\tilde{\theta}}s_{\tilde{\gamma}}\right)\left(\bar{V}_x+\tilde{V}_x\right) + \left(s_{\tilde{\theta}}s_{\tilde{\gamma}} - c_{\tilde{\theta}}c_{\tilde{\gamma}}\right)\tilde{V}_y\right) \tag{41h}$$

The parameters φ_γ and k_ρ belong to the sets $\Theta_1 = \mathbb{R}_{\geq 0}$ and $\Theta_2 = \mathbb{R}_{>0}$, respectively.

Proposition 3. *Let $\boldsymbol{\xi}$ be the state variable of a system that is UPAS on some parameter set Θ_3. Then the system (41) is UPAS on $\Theta_1 \times \Theta_2 \times \Theta_3$.*

Corollary 1. *The cascaded system (17), (25) and (41) is UPAS on the parameter set $\Theta_1 \times \Theta_2 \times \Theta_l$.*

Proof of Proposition 3. The system (41) will be treated as a cascade, where first practical stability of (41b) is established, and consequently that ρ can be bounded away from 0 such that the dynamics of $\tilde{\gamma}$ are valid. Then, (Orucevic, Wrzos-Kaminska et al., 2023, Theorem 2) is applied twice in succession to establish UPAS of the complete system.

Since the original variables ρ, γ are polar coordinates, ρ must be greater than zero, meaning that the dynamics (41) are only valid for $\tilde{\rho} \in (-\rho_d, \infty)$. Considering first the nominal part of (41b), $\dot{\tilde{\rho}} = f_2(\tilde{\rho}, k_\rho)$, it follows that since $k_\rho > 0$, the nominal dynamics are locally exponentially stable (LES). Consequently, by (Khalil, 2002, Theorem 4.12) there exists a Lyapunov function candidate for the system (41b) which satisfies (Orucevic, Wrzos-Kaminska et al., 2023, Assumption 3). Since $\bar{V}_x$, $\tilde{V}_x$, $\tilde{V}_y$ are bounded, $\boldsymbol{g}_2$ satisfies (Orucevic, Wrzos-Kaminska et al., 2023, Assumption 1), and $\boldsymbol{\xi}$ is the state of a system which is UPAS by assumption, by (Orucevic, Wrzos-Kaminska et al., 2023, Theorem 2), the system (41b) in cascade with the dynamics of $\boldsymbol{\xi}$ is UPAS on $\Theta_2 \times \Theta_3$.

Since the system (41b) in cascade with the dynamics of $\boldsymbol{\xi}$ is UPAS, by choice of $\tilde{\rho}(t_0)$ and parameters, it can be ensured that $|\tilde{\rho}(t)| < \rho_d$ s.t. $\rho(t) = \tilde{\rho}(t) + \rho_d \geq \rho_{\min} > 0\ \forall t \geq t_0$. Consequently, $\boldsymbol{g}_1$ satisfies (Orucevic, Wrzos-Kaminska et al., 2023, Assumption 1). Consider then the nominal part of the dynamics (41a), where $\tilde{\rho}$ is treated as time-varying signal. The following Lyapunov function candidate is chosen:

$$V_\gamma(\tilde{\gamma}) = \tfrac{1}{2}\tilde{\gamma}^2, \tag{42}$$

which gives

$$\begin{aligned}&\frac{\partial V_\gamma}{\partial t} + \frac{\partial V_\gamma}{\partial \tilde{\gamma}}f_2(\cdot)\\ &= \frac{1}{\tilde{\rho}+\rho_d}\tilde{\gamma}\left(-s_{\tilde{\gamma}}\left(\bar{V}_x+\tilde{V}_x\right) + c_{\tilde{\gamma}}\tilde{V}_y\right)\\ &= \frac{1}{\tilde{\rho}+\rho_d}\left(-\bar{V}_x|\tilde{\gamma}|\left|s_{\tilde{\gamma}}\right| + \left(c_{\tilde{\gamma}}\tilde{V}_y - s_{\tilde{\gamma}}\tilde{V}_x\right)\tilde{\gamma}\right)\\ &\leq \frac{1}{\rho_{\min}}\left(-\left(1-\alpha_1\right)\left(\bar{V}_x - \bar{V}_{x,\max}\right)|\tilde{\gamma}|\left|s_{\tilde{\gamma}}\right|\right.\\ &\quad\left. + \left(\left|c_{\tilde{\gamma}}\right|\tilde{V}_{y,\max} - \alpha_1\left(\bar{V}_x - \bar{V}_{x,\max}\right)\left|s_{\tilde{\gamma}}\right|\right)|\tilde{\gamma}|\right)\end{aligned} \tag{43}$$

where $\alpha \in (0,1)$. Let $\delta_1 = \arctan\left(\frac{\varphi_\gamma}{\alpha_1}\right)$, $\Delta_1 = \pi - \arctan\left(\frac{\varphi_\gamma}{\alpha_1}\right)$. Then,

$$\dot{V}_\gamma \leq -\frac{1}{\rho_{\min}}\left(1-\alpha_1\right)\left(\bar{V}_x - \bar{V}_{x,\max}\right)\sin(\delta_1)|\tilde{\gamma}|, \quad \forall \tilde{\gamma} \in H(\delta_1,\Delta_1) \tag{44}$$

where $H(\delta_1,\Delta_1) = \left\{\tilde{\gamma} \in \mathbb{R} \mid \delta_1 \leq |\tilde{\gamma}| \leq \Delta_1\right\}$. Since $\boldsymbol{\xi}$ is the state of a system which is UPAS by assumption, by (Orucevic, Wrzos-Kaminska et al., 2023, Theorem 2), the system (41) in cascade with the dynamics of $\boldsymbol{\xi}$ is UPAS on $\Theta_1 \times \Theta_2 \times \Theta_3$.

Proof of Corollary 1. By Proposition 2, the system (25) in cascade with (17) is uniformly globally practically asymptotically stable (UGPAS) on Θ_l. Then it follows from Proposition 3 that the complete cascaded system (17), (25) and (41) is UPAS on $\Theta_1 \times \Theta_2 \times \Theta_l$.

Remark 6. Since the nominal part of the dynamics (41b) is LES, there is no need (or possibility) of further diminishing the area to which $\tilde{\rho}$ converges in the nominal case. However, when the system (41b) is perturbed by another subsystem which is UPAS and therefore creates a generally nonvanishing disturbance, increasing k_ρ will help dominate the disturbance and decrease the area to which $\tilde{\rho}$ converges. Therefore, k_ρ is also included as a parameter when considering the practical stability of the complete system (41).

The domain on which the analysis in the proof of Proposition 3 is valid is illustrated in Fig. 3.

Remark 7. The controllers (35) and (39) can be applied to vehicles other than USRs, provided the vehicle is equipped with low-level controllers capable of (at least) practically asymptotically stabilizing the heading and velocity of the vehicle. The results of Proposition 3 can hold for states $\boldsymbol{\xi}$ consisting of other dynamic variables than those of the USR, so long as $\boldsymbol{\xi}$ contains $\tilde{v}_t, v_{n,\text{rel}}, \tilde{\theta}$ and that the dimensions of the interconnection terms $\boldsymbol{g}_1$, $\boldsymbol{g}_2$ in (41) are adjusted to match.

Remark 8. The parameter φ_γ is in practice not a freely adjustable control parameter, but a ratio of sizes of physical properties which influence the area to which the polar coordinate angle error $\tilde{\gamma}$ converges. The greater the smallest (i.e. worst-case) downstream current velocity $\bar{V}_x - \tilde{V}_{x,\max}$ is compared to the greatest sideways current $\tilde{V}_{y,\max}$, the smaller the area to which the polar angle error converges.

4. High-fidelity simulation

4.1. Coupled solver

This section briefly summarizes the algorithm simulating a planar articulated swimmer in a complex fluid environment with fluid–structure interaction which is used to validate the proposed control design in Section 5. The method is presented in Bernier et al. (2019) and relies on a computational fluid dynamics (CFD) solver coupled with a multi-body system (MBS) solver. First, the CFD solver is presented.

For the CFD solver, a vortex particle-mesh (VPM) technique is used. The VPM method solves the incompressible flow past deforming geometries by using the velocity–vorticity formulation of the Navier–Stokes equations,

$$\frac{D\omega_f}{Dt} = (\omega_f \cdot \nabla)\boldsymbol{u}_f + \nu\nabla^2\omega_f, \tag{45a}$$

where D/Dt denotes the Lagrangian derivative, $\boldsymbol{u}_f$ is the velocity field, ν is the kinematic viscosity and ω_f is the vorticity field. The method is summarized in Algorithm 1.

The first step in Algorithm 1 consists of recovering the velocity field from the vorticity field. Then, in the projection step, the fluid evolves as if the swimmer is absent. The resulting velocity field and position of particles, $\boldsymbol{u}_f^n$ and $\boldsymbol{x}$, are then used to predict the linear and angular momentum, $\boldsymbol{P}_{\text{proj}}$ and $\boldsymbol{I}_{\text{proj}}$, of the swimmer. The resulting forces and moments are given by $\boldsymbol{F}_{\text{proj}}$ and $\boldsymbol{M}_{\text{proj}}$, respectively. The hydrodynamical forces and moments are obtained through a mapping $\mathcal{F}$ and given by $\boldsymbol{\tau}_{\text{hyd}}$, while the actuation forces are given by $\boldsymbol{\tau}_{\text{act}}$. The MBS solver then computes the generalized coordinates given by $\boldsymbol{q} = [x_{\text{cm}}, y_{\text{cm}}, \theta_1, \phi_1, \ldots, \phi_{N_l-1}]^T$, where N_l is the number of links, from the equations of motion. An example configuration is shown in Fig. 4. The configuration is then translated into a characteristic function that describes the swimmer's shape χ_s through the mapping $\mathcal{G}$. The velocity field of the structure is represented by $\boldsymbol{u}_s$, which is found in a similar fashion through the mapping $\mathcal{H}$. The no-slip condition is then enforced by use of Brinkman penalization in (50a), resulting in the new velocity and vorticity fields, $\boldsymbol{u}_\lambda$ and ω_λ respectively. The forces and moments resulting from constraining the fluid, $\boldsymbol{F}_{\text{pen}}$ and $\boldsymbol{M}_{\text{pen}}$, are calculated in (50c) and (50d). Finally, the vorticity field is updated in (51a). Additionally, the time-step is constrained so that

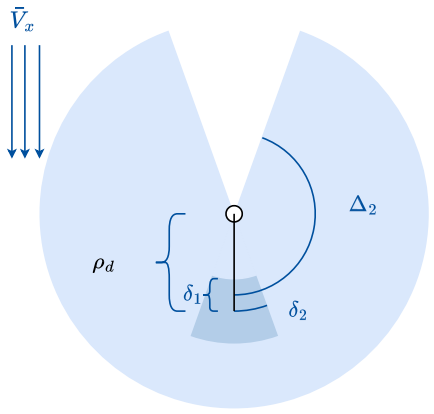

Fig. 3. Illustration of the area in which the analysis of the system (40) is valid (light blue) and the area to which the position converges (dark blue) . (For interpretation of the references to color in this figure legend, the reader is referred to the web version of this article.)

$\Delta t^n \leq \min\{C, h^2/2\nu, \Delta t^{\max}\}$ where $\Delta t^n = (t^{n+1} - t^n)$, C are the Lagrangian Courant–Friedrich–Levy conditions (LCFL) (Bernier et al., 2019), and h is the uniform spacing in the Cartesian discretization grid. The (LCFL) conditions may allow for time-steps that destabilize the MBS solver, therefore the time-step is constrained by a maximal time-step $\Delta t^{\max}$ which was found empirically.

While the CFD solver and the over-all architecture of the scheme is implemented as described by Bernier et al. (2019), the equations describing the swimmer dynamics in Bernier et al. (2019) are substituted with the USR dynamics formulation found in Kelasidi et al. (2016). The terms in the model of Kelasidi et al. (2016) associated with hydrodynamical effects are then replaced with the forces and moments computed in the CFD solver.

5. Results

This section presents results from a simulation study which was conducted in order to validate the performance of the proposed controller. The study is performed utilizing the high-fidelity simulation method described in Section 4, which faithfully captures the evolution of the fluid as well as the interaction between the fluid and the USR, in contrast to the simplified models which the control design and analysis are based on. For this reason, the controller's performance can be demonstrated with greater confidence when encountering complex, realistic fluid effects which it was not explicitly designed to handle. Moreover, one can observe how properties derived in the stability analysis carry over to the high-fidelity simulations.

5.1. Simulation setup

This section describes the parameters used during the simulations presented in this paper. The spatial domain is $[0, 3.0] \times [0, 3.0]$ with a discretization grid resolution of $[512, 512]$. For the velocity reference (39), $k_\rho = 0.2$ was chosen. The remaining parameters are shown in Table 1. The swimmer dimensions are illustrated in Fig. 5. A circular rigid body is placed in the center of the spatial domain, and a current is applied to the fluid, resulting in a vortex street forming downstream from the bluff body. The centroid of the bluff body is specified by $\left[x_{\text{cyl}}^{\text{cm}}, y_{\text{cyl}}^{\text{cm}}\right]^\top$. The Reynolds number chosen is $\text{Re} = \dfrac{\bar{V}_x D_{\text{cyl}}}{\nu} = 100$ for all simulations, where D_{cyl} is the diameter of the circular rigid body and the kinematic viscosity is given by ν. The Reynolds number for the cylinder is chosen rather than that of the particular swimmer to ensure consistent wake characteristics. It is desirable to have a standardized configuration of vortex shedding around the cylinder since it allows

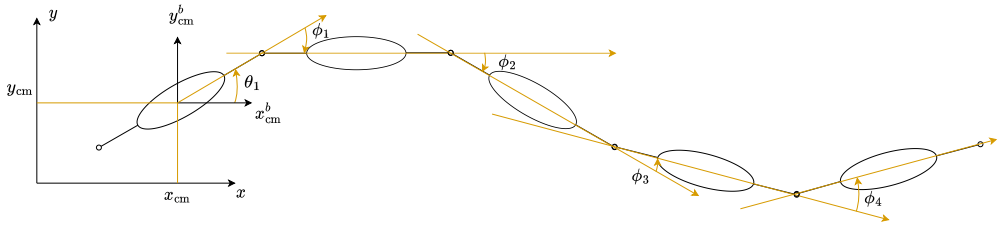

Fig. 4. Configuration of swimmer with five links.

Algorithm 1 Coupled Solver

While: $t^n \leq t^{\text{End}}$

1: Retrieve velocity field from vorticity field by solving the Poisson equation

$$\nabla^2 \boldsymbol{u}_f^n = -\nabla \times \omega_f^n. \tag{46}$$

2: Calculate projection forces and moments

$$\boldsymbol{P}_{\text{proj}}^{n+1} = \int_\Omega \rho_f \chi_s^n \boldsymbol{u}_f^n d\boldsymbol{x}, \qquad \boldsymbol{F}_{\text{proj}}^{n+1} = \frac{\boldsymbol{P}_{\text{proj}}^{n+1} - \boldsymbol{P}_{\text{proj}}^{n}}{\Delta t^n}, \tag{47a}$$

$$\boldsymbol{I}_{\text{proj}}^{n+1} = \int_\Omega \rho_f \chi_f^n (\boldsymbol{x} \times \boldsymbol{u}_f^n) d\boldsymbol{x}, \qquad \boldsymbol{M}_{\text{proj}}^{n+1} = \frac{\boldsymbol{I}_{\text{proj}}^{n+1} - \boldsymbol{I}_{\text{proj}}^{n}}{\Delta t^n}. \tag{47b}$$

3: Time integration of MBS and update swimmer position and velocity

$$\boldsymbol{\tau}_{\text{hyd}}^{n+1} = \mathcal{F}(\boldsymbol{F}_{\text{proj}}^{n+1} + \boldsymbol{F}_{\text{pen}}^{n}, \boldsymbol{M}_{\text{proj}}^{n+1} + \boldsymbol{M}_{\text{pen}}^{n}), \tag{48a}$$

$$\boldsymbol{\tau}_{\text{act}}^{n+1} \rightarrow \text{provided by a control law}, \tag{48b}$$

MBS solver computes $\boldsymbol{q}^{n+1}$ and $\dot{\boldsymbol{q}}^{n+1}$ for $t^{n+1} = t^n + \Delta t^n$ with the forces calculated.

$$\chi_s^{n+1} = \mathcal{G}(\boldsymbol{q}^{n+1}), \quad \boldsymbol{u}_s^{n+1} = \mathcal{H}(\boldsymbol{q}^{n+1}, \dot{\boldsymbol{q}}^{n+1}). \tag{49a}$$

4: Penalization of vorticity field and calculation of penalization forces and moments

$$\boldsymbol{u}_\lambda^{n+1} = \frac{\boldsymbol{u}^n + \lambda_f \Delta t^n \chi_s^{n+1} \boldsymbol{u}_s^{n+1}}{1 + \lambda_f \Delta t^n \chi_s^{n+1}}, \tag{50a}$$

$$\omega_\lambda = \nabla \times \boldsymbol{u}_\lambda^{n+1}, \tag{50b}$$

$$\boldsymbol{F}_{\text{pen}}^{n+1} = \int_\Omega \lambda_f \rho_f \chi_s^{n+1} (\boldsymbol{u}_\lambda^{n+1} - \boldsymbol{u}_s^{n+1}) d\boldsymbol{x}, \tag{50c}$$

$$\boldsymbol{M}_{\text{pen}}^{n+1} = \int_\Omega \lambda_f \rho_f \chi_s^{n+1} \boldsymbol{x} \times (\boldsymbol{u}_\lambda^{n+1} - \boldsymbol{u}_s^{n+1}) d\boldsymbol{x}. \tag{50d}$$

5: Time integration of vorticity field

$$\frac{\partial \omega_\lambda}{\partial t} = \nu \nabla^2 \omega_\lambda - \nabla \cdot (\boldsymbol{u}_\lambda \omega_\lambda) \tag{51a}$$

$$\omega_f^{n+1} = \omega_\lambda^{n+1} \tag{51b}$$

End while.

for the investigation of various swimmer sizes and control methods while maintaining a uniform environment. For a USR of a similar size to Mamba (Liljebäck, Stavdahl, Pettersen, & Gravdahl, 2014), the resulting kinematic viscosity becomes significantly higher than that of seawater. This choice was made for reasons of computational efficiency. However, the qualitative difference only becomes salient in the 3D case, where shedding occurs in cells along the height of the cylinder for $\text{Re} \in [300, 3 \cdot 10^5]$ (Sumer et al., 2006). Thus, the simulation with increased viscosity still captures the qualitative behavior of the vortex street. The dimensionless time is defined as $t^* = \frac{tU}{D_{\text{cyl}}}$ with the dimensionless unit

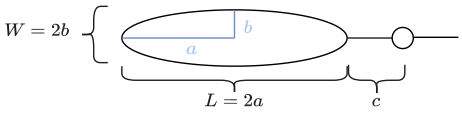

Fig. 5. Link and joint configuration.

s^*. A snapshot of the simulation of the USR in the wake can be seen in Fig. 11.

The control input in (16) requires exact knowledge of the hydrodynamical forces and moments that affect the USR when it operates in the wake. Measurements of these terms are not available in the high-fidelity simulation. This would also be the case in a real-life scenario, as there are no direct measurements of the forces and moments applied from the wake on the USR. Therefore, cancellation of hydrodynamical forces and moments is not implemented in the controller for this simulation study.

During initial tests for the simulation study, large deviations from the desired tangential velocity and desired distance to the bluff body were observed. This may be explained by unmodeled dynamics and disturbances that occur in the Von Karman vortex street. To combat this, integral action was added to the velocity reference generated by the high-level controller (39), using an integral gain $k_i = 0.01$. This addition and its relation to the theoretical analysis presented in Section 3 is further discussed in Section 5.2.

The initial tangential velocity of the USR is set to 0. This results in a large initial error between the desired tangential velocity and the initial tangential velocity, which demands a large virtual input $\ddot{\lambda}$. This can be interpreted as the rate of change in the frequency of the gait encoded by the joint references. Fast motion of the USR induces large vorticity spikes that propagate through the fluid environment, increasing the computational cost of the simulation. To avoid the extended computational time and disturbances in the vortex wake, a saturation, $\ddot{\lambda}_{\max} = 7\ \text{rad/s}^{*2}$, is imposed on $\ddot{\lambda}$. In a real-world scenario, this would likely only be part of an initial deployment procedure and only happen at the start of a mission.

Four simulation cases were investigated. Firstly, the USR was simulated with its initial position outside of the wake, with a static current direction. Secondly, the USR was simulated with its initial position in the wake, with the current direction rotating slowly. In the third case, the USR was simulated with its initial position in the wake, with the current direction rotating more quickly. Finally, the previous cases were combined in the fourth case, where the initial position of the USR was placed outside of the wake, and the direction of the current rotating. The rotation of the current is faster than in the second case but slower than in the third case.

5.2. Convergence to a wake with static current direction

The first scenario, where the USR starts outside of the wake, investigates the ability of the control law to stabilize the USR to the wake from relatively far away. This would correspond to the USR entering a wake initially, in order to initiate charging. This scenario is simulated both with and without adding integral effect to the forward velocity controller. Fig. 6 shows the results of the simulation case

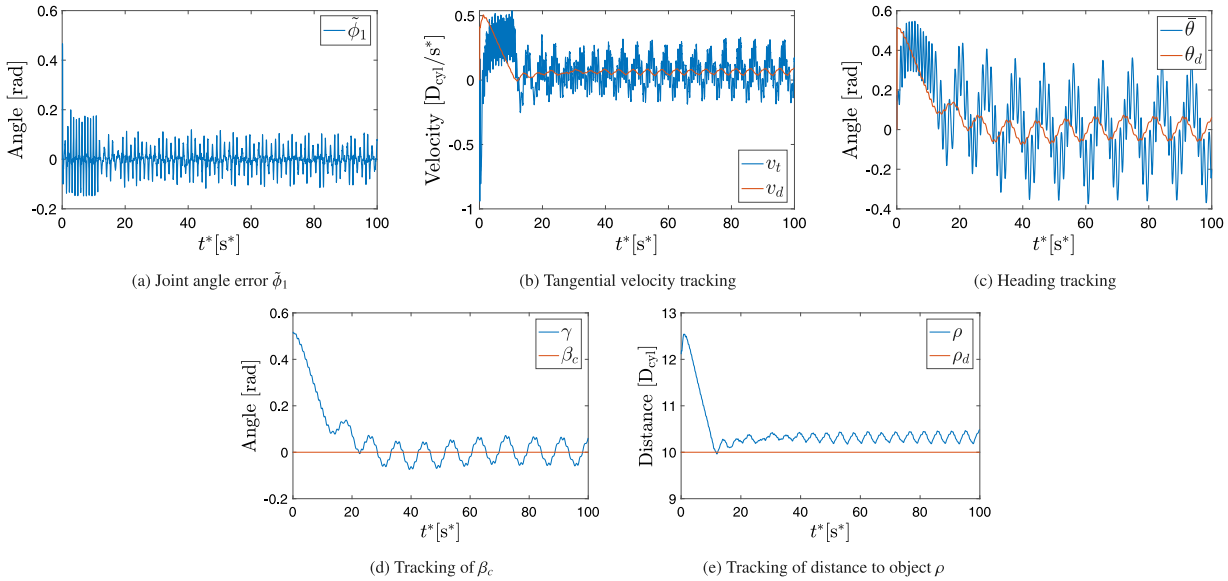

(a) Joint angle error $\tilde{\phi}_1$ (b) Tangential velocity tracking (c) Heading tracking

(d) Tracking of β_c (e) Tracking of distance to object ρ

Fig. 6. Plot of tracking for the low-level and high-level controllers without integral action in the case of regulation from outside a non-rotating wake.

without any integral effect. Fig. 6(a) to 6(c) demonstrate that the low-level control objectives of Section 2 are achieved. Specifically, Fig. 6(a) shows how the joint angles track their reference quite well. One may observe a small discrepancy between the joint angles and reference, which is in fact not strictly in keeping with Proposition 1. This may be explained by the complex hydrodynamical forces which were assumed to be canceled in the analysis. In the simulation these forces are not available for feedback, as would also be the case in a real-life scenario, and they provide a disturbance. However, the UGES property of the nominal control system guarantees a certain robustness in the presence of disturbances (Khalil, 2002, Lemma 9.1), resulting in the overall successful tracking of the joint references seen in Fig. 6(a). Moreover, Figs. 6(b) and 6(c) show how the heading and tangential velocity converge to a neighborhood of their respective references, in accordance with Proposition 2. In Fig. 6(a), only the first joint angle error is plotted for greater clarity, as the tracking in ϕ is similar for the remaining joint angles. Figs. 6(d) and 6(e) show the regulation of the high-level references for ρ and γ designed in Section 3. It is seen that γ converges to a neighborhood around β_c, and that ρ converges to a neighborhood around ρ_d, although a clear stationary deviation from the reference is observed in ρ. This is to be expected, as the velocity reference attempts to counteract the unmodeled disturbance from the current without any integral action. Still, the high-level control objectives are achieved in accordance with Proposition 3, as ρ converges within some neighborhood of ρ_d. In the case of a steady-state offset, the result of Proposition 3 formally states that a greater proportional gain will reduce the steady-state offset but not necessarily remove it entirely. This motivates the addition of an integral term to the control law (39) in the next simulation.

In Fig. 7, the performance of the controller with integral action in forward velocity is shown in the same scenario. For the low-level control objectives in Fig. 7(a) to 7(c) as well as for γ in Fig. 7(d), the performance is comparable with that of the controller without integral action seen in Fig. 6. However, in Fig. 7(e) it is shown that ρ converges to a significantly smaller neighborhood of ρ_d than is seen in Fig. 6(e). While a stationary error is observed in the case without integral action, in Fig. 7(e) it can instead be seen that after an initial reaching phase, a steady-state behavior is achieved where the radius oscillates around the reference. Both this and the offset present without the integral action are within the realm of expected behavior of a UPAS system, since they are both examples of the state converging to and remaining within a neighborhood of the reference. However, the integral action has not been included in the analysis in Section 3. Integral action is typically used to combat constant disturbances, in which case an integral state can often be shown to converge to a value exactly offsetting the disturbance. In the presence of a time-varying disturbance, and when the other states are practically stable rather than converging to an exact value, it is difficult to determine what value an integral state would converge towards and subsequently what stability properties the resulting system might have. However, it can be argued that even if the radius is UPAS regardless of integral action, oscillation around the reference is a more desirable steady-state behavior than oscillation around an offset point for the given application. While the error could also be reduced by increasing the proportional gain instead of adding an integral term, a very large proportional gain can result in an excessive and unrealistic velocity reference in response to large initial errors. Thus, the integral action improves the controller performance significantly in practice in the given scenario.

To summarize, the success of the cascaded controller in stabilizing both γ and ρ to a vicinity of their references demonstrates the ability of the controller to automatically align the USR with the wake without knowledge of the ocean current's direction or magnitude. The control laws as implemented in the simulation do not rely on cancellation of hydrodynamical terms which are difficult to measure or estimate in practice, making these results promising with regards to a potential future practical implementation.

5.3. Tracking of a wake in slowly rotating current direction

This section presents the results from the simulations with the USR starting within the wake, with the current direction rotating slowly. This scenario investigates the ability of the control law to track changes in the wake that occur if the direction of the greater ocean current varies, even though the control law was developed under the premise of a constant current direction. The current direction is kept constant until $t^* = 10$ in order to allow the formation of a vortex street prior to rotating the direction. Fig. 8(a) to 8(c) demonstrate that the low-level control objectives of Section 2 are achieved. Specifically, Fig. 8(a) demonstrates that the joint angles converge to their references in accordance with Proposition 1, although small discrepancies can be observed. Again, as in the case of a static wake, these discrepancies are explained by the unmeasured hydrodynamical effects which are not accounted for during analysis. For clarity, again only the first joint angle error $\tilde{\phi}_1$ is plotted, as the remaining joint angle errors exhibit

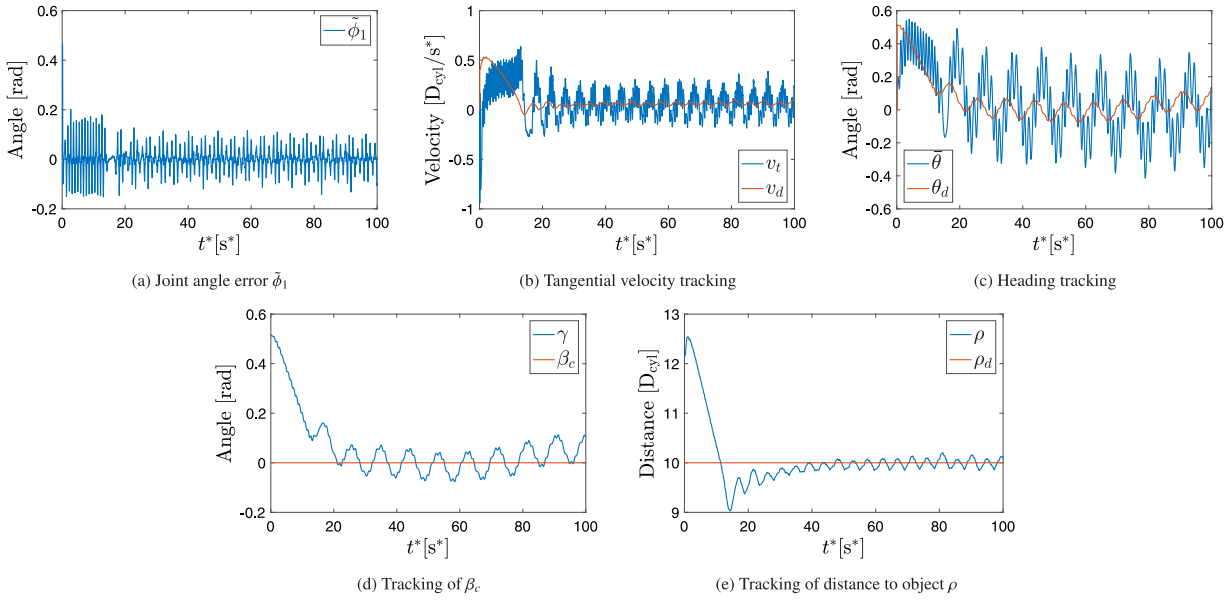

(a) Joint angle error $\tilde{\phi}_1$ (b) Tangential velocity tracking (c) Heading tracking

(d) Tracking of β_c (e) Tracking of distance to object ρ

Fig. 7. Plot of tracking for the low-level and high-level controllers with integral action in the case of regulation from outside a non-rotating wake.

similar behavior. Moreover, Figs. 8(b) and 8(c) show how the heading and tangential velocities converge to a neighborhood of their respective references, in accordance with Proposition 2. Furthermore, the heading is shown to track the moving reference quite closely during the rotating ocean current.

Figs. 8(d) and 8(e) show the tracking of the high-level control objectives from Section 3. Specifically, ρ is shown to converge to a neighborhood around its reference, although some greater fluctuation is seen here than in Fig. 7(e). Moreover, while the current now rotates at non-zero rate, unlike what the error dynamics (37) are based on, γ still tracks its moving reference β_c quite well, although some phase lag is observed. This is to be expected, as the controller is designed for a stationary direction, and has to reactively correct for changes without any knowledge of the motion. In addition, the USR has no actuation in its normal direction, in which it has to move to track the wake. Instead, it is pushed by the ocean current, which has little to no contribution along the tangent of the circle when the USR is aligned with the wake. Thus a deviation from the center line must occur in order for a restoring force to appear. For the considered energy-harvesting application this phase lag is acceptable as long as the USR ends up stabilizing itself in the middle of the street when the current is no longer rotating. The change in direction of an ocean current is expected to be far slower in a real-world application than in the simulation scenario presented here. The controller achieves the control objective even in this exaggerated scenario. This is promising with regards to a real-life scenario.

5.4. Tracking of a wake in current with quicker change of direction

This section presents the results from the simulations with the USR starting within the wake, with the current direction rotating more quickly. This scenario is included to investigate the limits of the ability of the control law to track changes in the vortex wake under conditions which are far from the premises of the theoretical analysis. The current direction is kept constant until $t^* = 10$ in order to allow the formation of a vortex street prior to the direction rotating. Fig. 9 show the results from the simulation case. The simulation is run for an entire revolution of the current. Fig. 9(a) shows that the joint controller tracks the reference well, in accordance with Proposition 1. As in previous cases, there are small discrepancies which, while contradicting the UGES claim of Proposition 1, can be explained by unmodeled hydrodynamical forces. Figs. 9(b) and 9(c) demonstrate that the velocity and heading controllers to a large extent, achieve convergence to neighborhoods of their references, with the exception of the velocity controller during the first 20 s of the simulation. The failure to achieve convergence to the reference during this period is caused by the saturation imposed on $\ddot{\lambda}$ during simulations. However, after the first 20 s^*, the tangential velocity converges to a neighborhood of the desired tangential velocity.

Figs. 9(d) and 9(e) demonstrate that the controller still retains the ability to track the position references to a certain extent, although performance is degraded when compared to the previous observed cases. In Fig. 9(d) it is shown that γ still remains within a neighborhood following the reference value, although with a more pronounced phase lag. However, Fig. 9(e) shows that while ρ at times converges to a neighborhood of the reference, it also drifts a little away at times. By the end of the simulated time, the current again comes from its initial direction. The performance is not expected to improve nor reach a steady-state if simulated for a longer time over several revolutions of the current, since this scenario is outside of the expected operating conditions for the developed controller. Looking again at Fig. 9(e), it is of particular interest that the drift away from the desired radius occuring at around 55–70 s^* coincides with the largest experienced heading errors, as can be seen in Fig. 9(c). The heading error disturbs the position dynamics due to the interconnection of the control layers. In addition, the velocity reference (39) is scaled down when there is a heading error, i.e. when the USR does not point directly towards the bluff body. While this can help avoid the unnecessary control of swimming in the wrong direction, it means that performance of the control of radius is reduced until the desired heading is reached again.

It should be noted here that this case significantly violates the premise that the direction of the current is constant, on which the error dynamics and hence stability analysis of γ are based. As such some degradation of performance and loss of stability properties are to be expected. Taking this into consideration, the controller seems to retain the ability to achieve the control objectives fairly well. In addition, if the current changes its direction too fast for the USR to follow, the USR risks ending up in a situation where it needs to swim with the current, violating Assumption 2. If the USR is required to swim with the current, the current itself might be fast enough to meet the total reference velocity, in which case the controller would cause the USR to slow down or even stop swimming and drift with the current. If the USR stops actively swimming, it also loses the ability to turn, similarly to a ship with a rudder. This further hinders the USR from recovering.

Overall, both the low-level and high-level controllers track their references quite well, demonstrating the UPAS properties of the system

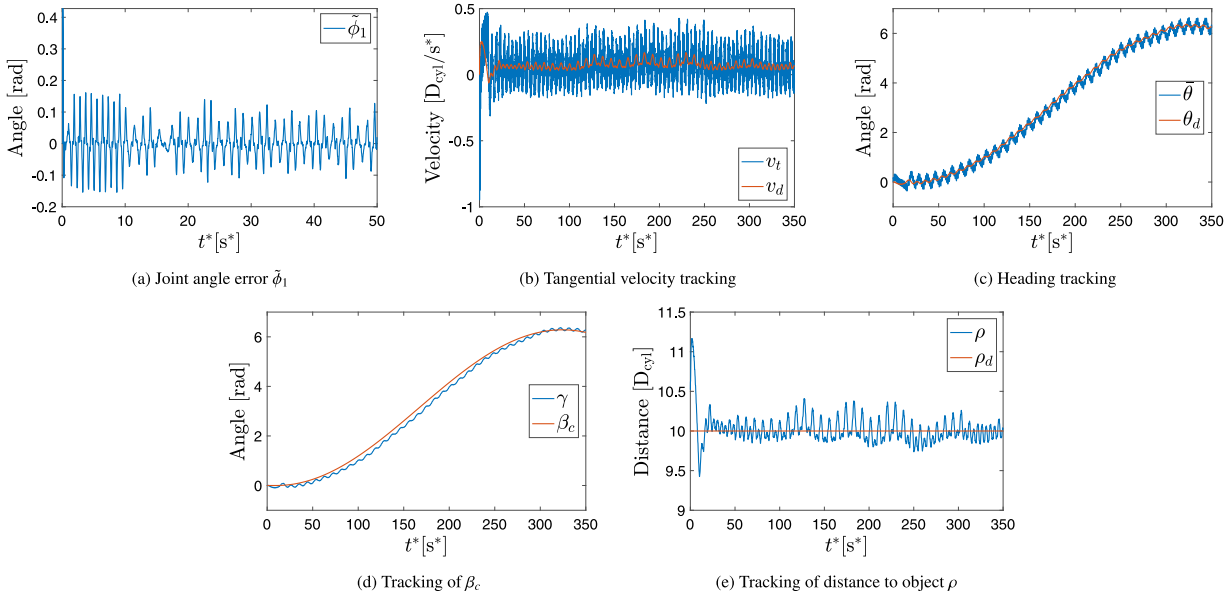

(a) Joint angle error $\tilde{\phi}_1$ (b) Tangential velocity tracking (c) Heading tracking

(d) Tracking of β_c (e) Tracking of distance to object ρ

Fig. 8. Plot of tracking for the low-level and high-level controllers in the case of a slowly rotating wake.

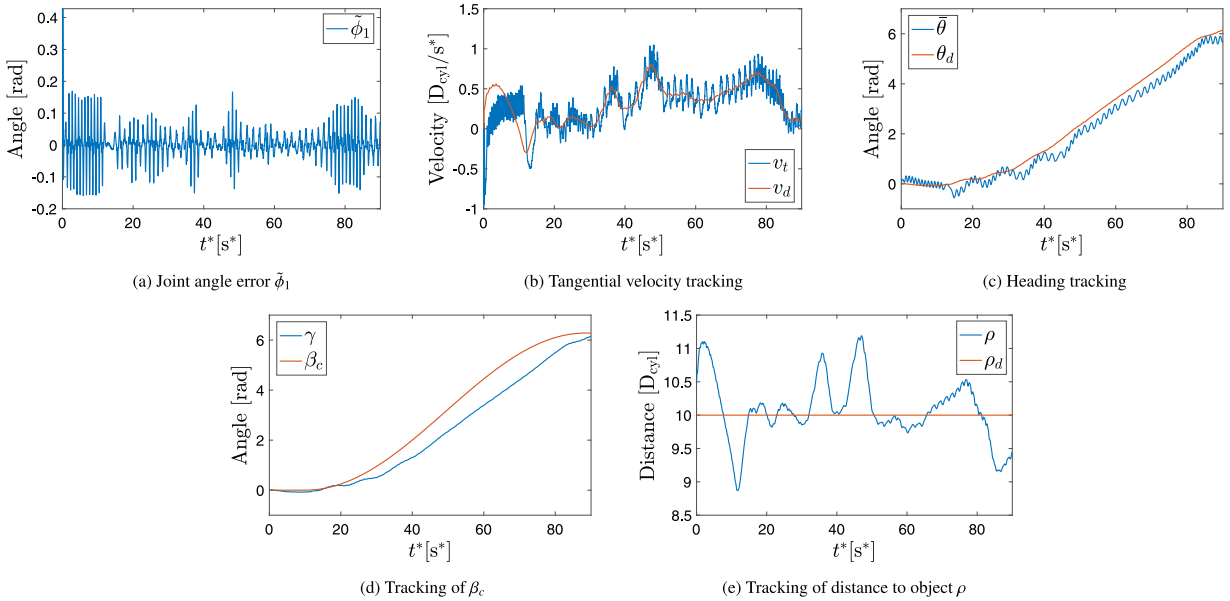

(a) Joint angle error $\tilde{\phi}_1$ (b) Tangential velocity tracking (c) Heading tracking

(d) Tracking of β_c (e) Tracking of distance to object ρ

Fig. 9. Plot of tracking for the low-level and high-level controllers in the case of a quickly rotating wake.

as a whole. Given the high-fidelity simulations which were carried out to verify the controller performance, and given the low reliance of the controller on model knowledge, these simulations appear greatly promising for the method's efficacy in experiments and transfer to real-world use cases.

5.5. Tracking of a wake with rotating current direction and initial position outside of wake

This section presents the results from the simulations with the USR starting outside of the wake and a rotating current direction. The rotational velocity of the current is selected to be faster than the second case but slower than the third case. This is done to investigate the behavior of the USR with the suggested controller when all the conditions of the previous cases are combined. The direction of the current is kept constant until $t^\star = 4.0$ to allow for the formation of the vortex wake. The time before the current direction rotates is shortened in order for the current to change direction before the USR reaches the vortex wake.

The simulation results are shown in Fig. 10. Fig. 10(a) shows the joint tracking error for the first joint, and as in the previous cases the joint controller is shown to track the reference well. Interestingly, the tracking error decreases at around the same time as the tangential velocity and its reference, shown in Fig. 10(b), decrease from their initial, higher values. In other words the joint tracking improves as the reference gait stabilizes to a slower frequency. The gait frequency slows down after the USR achieves the desired position and starts to maintain a steady position against the current. Figs. 10(c) and 10(d) show that both the heading and γ have an initial converging phase after which they track their desired values reasonably well, but with a slight delay. This is to be expected, especially in the case of γ, since the controller is designed for a stationary direction and will therefore exhibit some delay in tracking a moving direction. Compared to the two previous cases with a rotating wake, γ is shown to lag further behind

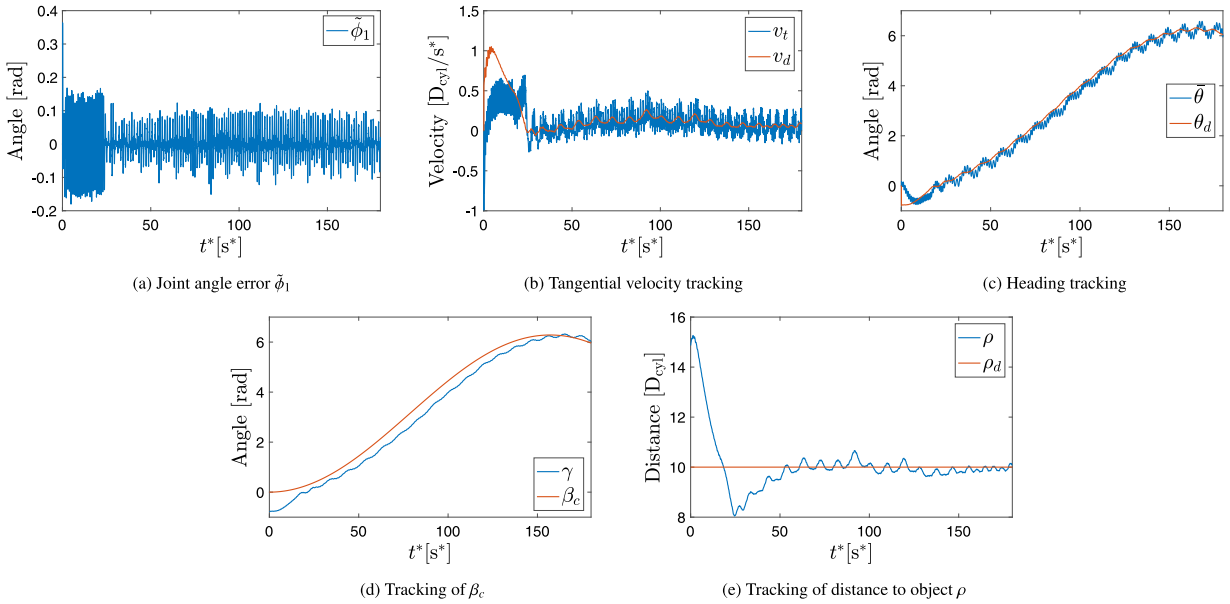

(a) Joint angle error $\tilde{\phi}_1$ (b) Tangential velocity tracking (c) Heading tracking

(d) Tracking of β_c (e) Tracking of distance to object ρ

Fig. 10. Plot of tracking for the low-level and high-level controllers in the case of a rotating current and USR with initial conditions outside of the wake.

Table 1
Simulation parameters.

$\bar{V}_x$	D_{cyl}	a	b	c	ρ_f	ρ_s	C	Δt^{max}	x_{cyl}^{cm}	y_{cyl}^{cm}	k_ρ	k_i
$2.0D_{cyl}/s^*$	0.1	$0.3125D_{cyl}$	$0.2a$	$0.1D_{cyl}$	997	997	0.02	0.001	1.5	1.5	0.2	0.01

β_c now, in Fig. 10(d), than in Fig. 8(d), but not as much as in Fig. 9(d), which is as expected when the wake now rotates at a speed between the two previous cases. Fig. 10(d) also shows that as the rotation slows down towards the end of the simulated time, γ converges closer to β_c. Fig. 10(e) shows that after an initial overshoot, the radius converges to a neighborhood of its desired value. The overshoot is larger than in the case of converging to a stationary wake in Fig. 7(e), but is worth noting that the initial state in Fig. 10(e) is also further away from the reference than the one in Fig. 7(e).

Overall, the controller manages its objective of reaching and tracking the wake well also in the case of having to converge towards a rotating wake. It is worth repeating that both the speed at which the current rotates, as well as the starting time of the rotation had to be made faster compared to the case in Section 5.3, in order for the wake to start moving away from the USR before the USR has converged to the vicinity of the wake. Taken together with the fact that the current rotation was unrealistically fast already in the previous scenario in Section 5.3, this demonstrates that the system dynamics with the proposed controller are sufficiently fast compared to the environmental effects it is designed to adjust to.

5.6. Investigation of the impact of UPAS-parameters on the radius of convergence

The UPAS property which has been derived for the closed-loop system in Section 3 implies that the area of convergence for the state can be altered by adjusting the parameters $\boldsymbol{\varphi}_l$, k_ρ, φ_γ. It is important to verify that these properties, which are proven with simplified dynamical models, still hold for the closed-loop system with a high-fidelity description of the system dynamics. To this end, a simulation study was conducted, investigating the effect of the parameter k_ρ on the radius of convergence of (41b). The USR is initially in a vortex wake with a static direction, further away from the cylinder than ρ_d. The simulation is performed with different proportional gains $k_\rho \in [0.1, 0.2, 0.4]$. Fig. 12 shows the resulting plots of ρ for different values of k_ρ. The results show that the simulations with pure proportional action converge to neighborhoods around ρ_d whose radii decrease with increasing values of k_ρ, which is in accordance with the previously stated property of UPAS systems. This demonstrates that the model and method used for analysis are sufficient to capture properties of the more complex model and the high-fidelity simulation described in Section 4. This is again promising for the control system's performance in real-world experiments and applications, as the high-fidelity simulation captures complex fluid effects that are not explicitly accounted for during analysis.

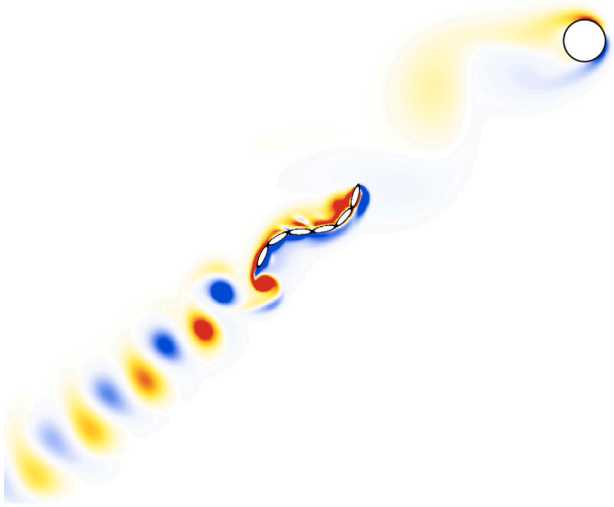

Fig. 11. Snapshot from the simulation of the USR in a vortex street.

6. Conclusions and future work

In this paper, the automatic alignment of a USR with the wake behind a bluff body was investigated. A cascaded controller was derived

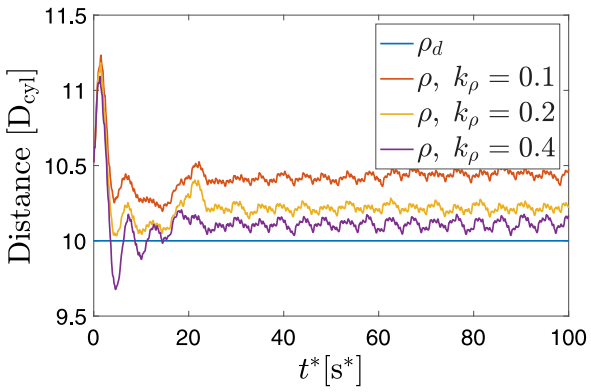

Fig. 12. Tracking of distance to object ρ for different values of k_ρ. For the case with integral effect, $k_i = 0.05$.

and the resulting closed-loop system was proven to be UPAS. Furthermore, the performance of the controller was verified through high-fidelity simulations of the USR-fluid system. The simulations successfully verified the theoretical properties of the controller, and demonstrated the efficacy of the controller both in stabilizing the USR to a vortex wake from outside of it, as well as in tracking changes in the wake direction due to rotations in the larger current direction.

The high fidelity of the simulations carried out, as well as the low requirements of model knowledge in the development of the controller, make these results promising with respect to the controller's performance in experiments and real-world scenarios. While the control method presented in this paper is suited for positioning a USR in the wake behind an object, much work still remains before the overarching goal of energy autonomy can be achieved. This includes the development of both control methods and hardware which will allow the USR to go from consuming energy for stationkeeping to harvesting energy from the wake.

CRediT authorship contribution statement

Amer Orucevic: Writing – review & editing, Writing – original draft, Visualization, Validation, Software, Methodology, Investigation, Formal analysis, Data curation, Conceptualization. **Marianna Wrzos-Kaminska:** Writing – review & editing, Writing – original draft, Visualization, Validation, Software, Methodology, Formal analysis, Data curation, Conceptualization. **Mads Erlend Bøe Lysø:** Writing – review & editing, Writing – original draft, Visualization, Validation, Software, Methodology, Investigation, Formal Analysis, Data curation, Conceptualization. **Kristin Ytterstad Pettersen:** Writing – review & editing, Writing – original draft, Supervision, Conceptualization. **Jan Tommy Gravdahl:** Writing – review & editing, Writing – original draft, Supervision, Conceptualization.

Declaration of competing interest

The authors declare that they have no known competing financial interests or personal relationships that could have appeared to influence the work reported in this paper.

Acknowledgment

The authors would like to thank Torleiv H. Bryne for providing insightful ideas regarding the application of WOPC.

References

Allen, J. J., & Smits, A. J. (2001). Energy harvesting eel. *Journal of Fluids and Structures*, *15*(3–4), 629–640.

Bernier, C., Gazzola, M., Chatelain, P., & Ronsse, R. (2018). Numerical simulations and development of drafting strategies for robotic swimmers at low Reynolds number. In *Proc. IEEE international conf. biomedical robotics and biomechatronics*.

Bernier, C., Gazzola, M., Ronsse, R., & Chatelain, P. (2019). Simulations of propelling and energy harvesting articulated bodies via vortex particle-mesh methods. *Journal of Computational Physics*, *392*, 34–55.

Caharija, W., Pettersen, K. Y., & Gravdahl, J. T. (2013). Counter-current and co-current guidance of underactuated unmanned marine vehicles. In *Proc. 2013 IFAC intel. auton. vehicles symp.*. Gold Coast, Australia.

Fossen, T. I., & Strand, J. P. (2001). Nonlinear passive weather optimal positioning control (WOPC) system for ships and rigs: experimental results. *Automatica*, *37*(5), 701–715.

Kelasidi, E., Liljebäck, P., Pettersen, K. Y., & Gravdahl, J. T. (2016). Innovation in underwater robots: Biologically inspired swimming snake robots. *IEEE Robotics & Automation Magazine*, *23*(1), 44–62.

Kelasidi, E., Pettersen, K. Y., Gravdahl, J. T., Stromsoyen, S., & Sorensen, A. (2017). Modeling and propulsion methods of underwater snake robots. In *2017 IEEE conf. on control technology and applications* (pp. 819–826). Mauna Lani Resort, HI, USA: IEEE.

Khalil, H. K. (2002). *Nonlinear systems* (3rd ed.). Prentice-Hall.

Kim, Y.-S., Kim, J., & Sung, H.-G. (2016). Weather-optimal control of a dynamic positioning vessel using backstepping: simulation and model experiment. *IFAC-PapersOnLine*, *49*(23), 232–238, 10th IFAC Conference on Control Applications in Marine Systems (CAMS) 2016.

Kjerstad, Ø. K., & Breivik, M. (2010). Weather optimal positioning control for marine surface vessels. In *Proc. 8th IFAC conf. control appl. marine syst.*. Rostock-Warnemünde, Germany.

Kohl, A. M., Kelasidi, E., Mohammadi, A., Maggiore, M., & Pettersen, K. Y. (2016). Planar maneuvering control of underwater snake robots using virtual holonomic constraints. *Bioinspiration & Biomimetics*, *11*(6).

Kohl, A. M., Kelasidi, E., Pettersen, K. Y., & Gravdahl, J. T. (2015). A control-oriented model of underwater snake robots exposed to currents. In *Proc. IEEE conf. control applications*.

Kohl, A. M., Pettersen, K. Y., Kelasidi, E., & Gravdahl, J. T. (2015). Analysis of underwater snake robot locomotion based on a control-oriented model. In *Proc. conf. robot. biomim.* (pp. 1930–1937). Zhuhai, China.

Lapierre, L., & Jouvencel, B. (2005). Path following control for an eel-like robot. *Vol. 1*, In *Proc. Europe oceans 2005* (pp. 460–465). http://dx.doi.org/10.1109/OCEANSE.2005.1511759, Vol. 1.

Liljebäck, P., Pettersen, K. Y., Stavdahl, Ø., & Gravdahl, J. T. (2010). Controllability and stability analysis of planar snake robot locomotion. *IEEE Transactions on Automatic Control*, *56*(6), 1365–1380.

Liljebäck, P., Stavdahl, Ø., Pettersen, K. Y., & Gravdahl, J. T. (2014). Mamba - a waterproof snake robot with tactile sensing. In *2014 IEEE/RSJ international conference on intelligent robots and systems* (pp. 294–301).

Mohammadi, A., Rezapour, E., Maggiore, M., & Pettersen, K. Y. (2016). Maneuvering control of planar snake robots using virtual holonomic constraints. *IEEE Transactions on Control Systems Technology*, *24*(3), 884–899.

Orucevic, A., Gravdahl, J. T., Pettersen, K. Y., & Chaillet, A. (2022). Uniform practical asymptotic stability for position control of underwater snake robots. In *Proc. 2022 IEEE conf. control technol. appl.*. Trieste, Italy.

Orucevic, A., Lysø, M. E. B., Schmidt-Didlaukies, H., Pettersen, K. Y., & Gravdahl, J. T. (2023). Optimal positioning of snake robots in vortex wakes using extremum-seeking control. In *Proc. 22nd IFAC world congress*. Yokohama, Japan.

Orucevic, A., Wrzos-Kaminska, M., Gravdahl, J. T., & Pettersen, K. Y. (2023). Uniform practical asymptotic stability for position control of underwater snake robots. *IEEE Transactions on Control Systems Technology*, http://dx.doi.org/10.1109/TCST.2023.3345211.

Pettersen, K. Y. (2017). Snake robots. *Annual Reviews in Control*, *44*, 19–44.

Pinkster, J. A., & Nienhuis, U. A. (1986). Dynamic positioning of large tankers at sea. In *Proc. offshore technology conference*.

Sumer, B. M., et al. (2006). *Hydrodynamics around cylindrical strucures*: *vol. 26*, World scientific.

Wiens, A. J., & Nahon, M. (2012). Optimally efficient swimming in hyper-redundant mechanisms: control, design, and energy recovery. *Bioinspiration & Biomimetics*, *7*(4), http://dx.doi.org/10.1088/1748-3182/7/4/046016.